Review of Shock-Turbulence Interaction with a Focus on Hypersonic Flow

Alberto Cuadra,[1] Mario Di Renzo,[2,3] Jimmy-John O.E. Hoste,[4] Christopher T. Williams,[3] Marcos Vera,[1] and César Huete[1, a)]

[1)] *Grupo de Mecánica de Fluidos, Departamento de Ingeniería Térmica y de Fluidos, Universidad Carlos III de Madrid, Leganés 28911, Spain*

[2)] *Department of Engineering for Innovation, University of Salento, Lecce 73100, Italy*

[3)] *Center for Turbulence Research, Stanford University, Stanford, 94305, USA*

[4)] *Destinus SA, Payerne, Switzerland*

(Dated: 17 February 2025)

Hypersonic flight involves a variety of complex flow phenomena that directly impact the aerothermodynamic loading of high-speed vehicles. The turbulence encountered during a typical flight trajectory influences and interacts with the shock waves on and around the surface of a vehicle and its propulsion system, affecting both aerodynamic and power plant performance. These interactions can be studied by isolating a turbulent flow convected through a normal shock, commonly referred to as the canonical shock-turbulence interaction (STI) problem. Scale-resolving computational fluid dynamics (CFD) and linear interaction analysis (LIA) have been crucial in studying this problem and formulating scaling laws that explain the observed behavior. In this work, an extensive review of the theoretical (LIA) and numerical (CFD) work on the canonical STI is presented. The majority of the work conducted to date has focused on calorically perfect gases with constant heat capacities. However, in hypersonic flows, chemical and thermal non-equilibrium effects may alter the nature of the interaction. As a result, relevant LIA and CFD studies addressing high-enthalpy phenomena are also succinctly discussed.

NOMENCLATURE

Roman Symbols

ℓ	Integral length scale of the upstream turbulence
ℓ_T	Thickness of the post-shock thermochemical nonequilibrium region
$\mathcal{I}$	Turbulent intensity
$\mathcal{K}$	Similarity parameter
$\mathcal{P}$	Pressure ratio
$\mathcal{R}$	Density ratio
$\mathcal{T}$	Temperature ratio
$\mathcal{U}$	Post-shock streamwise velocity perturbation amplitude
$\mathcal{V}$	Post-shock spanwise velocity perturbation amplitude
$\mathcal{V}_{ij}^{\mathrm{SGS}}$	Subgrid viscous stress
$\mathcal{W}$	O_2 to N_2 molecular weight ratio
Da	Damköhler number
L_λ	Taylor microscale length
P	Probability-density distribution
Re_ℓ	Turbulent Reynolds number
Re_λ	Taylor microscale Reynolds
$\widetilde{S}_{ij}$	Favre-averaged strain-rate tensor
c	Speed of sound
c_p	Specific heat at constant pressure
c_v	Specific heat at constant volume
d	Degrees of freedom
E	Energy spectrum
e	Internal energy
h	Enthalpy
K	Turbulent kinetic energy amplification factor
k	Wavenumber amplitude
k_o	Characteristic wavenumber
P	Pressure
R_g	Specific gas constant
R_{ij}	Reynolds' stress tensor
T	Temperature
t	Time
u	Streamwise/longitudinal velocity
v	Spanwise/transverse velocity
W	Molecular weight
X	Molar fraction
x, y, z	Spatial coordinates
Y	Mass fraction
$\mathcal{M}_1$	Shock Mach number
$\mathcal{M}_t$	Turbulent Mach number
$\mathbf{k}$	Wavenumber vector
$\mathbf{v}$	Velocity vector

Greek Symbols

β	Downstream to upstream sound speed ratio
χ	Upstream entropic to rotational perturbation amplitude ratio

[a)] Electronic mail: chuete@ing.uc3m.es

δ_ν	Thickness of the post-shock viscous dissipation region
δ_{vib}	Thickness of the post-shock vibrational relaxation region
η	Upstream dilatational to solenoidal kinetic energy ratio
η'	Upstream dilatational to total kinetic energy ration
η_k	Kolmogorov length scale
Γ	Normalized slope of the Hugoniot curve
γ	Adiabatic index, or heat capacity ratio
$\hat{\sigma}_{ij}$	Viscous stress tensor
μ	Dynamic viscosity
ν	Kinematic viscosity
ω	Vorticity
Φ	Energy spectrum tensor
ϕ	Phase angle
ρ	Density
τ	Dimensionless time
τ_{ij}^{SGS}	Subgrid stress tensor
Θ	Characteristic temperature
θ	Wave angle
ε_a	Upstream acoustic perturbation amplitude
ε_e	Upstream entropic perturbation amplitude
ε_r	Upstream rotational perturbation amplitude
ξ_s	Shock displacement
ζ	Frequency
$\boldsymbol{\omega}$	Vorticity vector

Subscripts and superscripts

1	Upstream condition
2	Downstream condition
a	Acoustic
e	Entropic
r	Rotational
vib	Vibrational

Acronyms

rms	Root mean square
CEA	Chemical Equilibrium with Applications
CFD	Computational Fluid Dynamics
CFL	Courant-Friedrichs-Lewy
CPU	Central Processing Unit
CT	Combustion Toolbox
DNS	Direct Numerical Simulation
DSM	Dynamic Smagorinsky Model
ENO	Essentially-Non-Oscillatory
EoS	Equation of State
FD	Finite-Difference
GPU	Graphics Processing Unit
HIT	Homogeneous Isotropic Turbulence
HTR	Hypersonic Task-based Research
ISA	International Standard Atmosphere
LES	Large Eddy Simulation
LIA	Linear Interaction Analysis
NASA	National Aeronautics and Space Administration
NASP	National Aerospace Plane
RANS	Reynolds-Averaged Navier-Stokes
RH	Rankine-Hugoniot
SDT	Spatially Developed Turbulence
SGS	Subgrid-Scale
STI	Shock-Turbulence Interaction
TENO	Targeted Essentially Non-Oscillatory
TKE	Turbulent Kinetic Energy
WENO	Weighted-ENO

I. INTRODUCTION

Hypersonic flows encompass a wide range of complex physical phenomena, including shock waves, chemical and thermal non-equilibrium, radiation, and plasma formation.[1] In the continuum flow regime, turbulence may also play a major role. For instance, hypersonic vehicles such as the National Aerospace Plane (NASP) are expected to develop turbulent boundary layers along their flight trajectory, as illustrated in Fig. 1 of Settles and Dodson.[2] Accurately capturing the effects of turbulence and its interaction with these phenomena, particularly shock waves, is crucial for assessing reliable predictions of hypersonic vehicle performance throughout the entire mission.

As pointed out by Theofilis *et al.*,[3] the least understood region of the flight envelope ranges from 40 to 70 km in altitude, where thermochemical non-equilibrium effects can be relevant. In order to further a fundamental understanding of these types of flows, turbulence must be described through scale-resolving simulations, which introduce substantial challenges for computational fluid dynamics (CFD). In addition to the high demands on CPU/GPU resources and the limitations of current computational architectures, there is a critical need to develop numerical methods and frameworks that can effectively capture the combined effects of turbulence, shock waves, and thermochemical processes. The need for CFD-based studies on hypersonics is apparent, as experimentally reproduced equivalent flight conditions are strongly dependent on the type of test facility and the associated test time limitations.[4,5]

Research codes specifically tailored to a set of physics of interest have historically been used for fundamental studies. For example, the Hybrid code[6,7] was developed with turbulence and shock waves in mind, with the spatial discretization implemented using high-resolution

finite-difference schemes. In recent years, new such finite-difference numerical frameworks were developed taking advantage of the rapidly evolving GPU architectures.[8–13] These developments are key in enabling the study of more complex hypersonic flow problems by continuously pushing the boundaries of flow conditions (Reynolds number) and multi-physics (degrees of freedom). This has led to an increased interest in scale-resolving studies of turbulent shock wave/boundary layer interactions[14–17] as well as hypersonic boundary layers with thermochemical effects[10,15,18]. In these studies, it is crucial to isolate the various thermo-physical flow phenomena involved in order to draw meaningful conclusions, as exemplified by Larsson *et al.*[19] Thus, while boundary layers play a key role in the aero-thermomechanical design of hypersonic vehicles and associated heat management,[20] the fundamental interaction between shock waves and turbulence also warrants analysis through isolated studies.

The canonical shock-turbulence interaction (STI) problem can be considered the simplest representation of turbulence interacting with a shock wave, isolating the physics from surrounding effects such as boundary layers, cross-flows, or traveling pressure waves induced by combustion. As depicted in Fig. 1, this setup provides a controlled environment to investigate fundamental physics relevant to supersonic and hypersonic flows. The advent of accessible computational resources, starting in the early 1990s, has enabled the use of scale-resolving simulations to further our understanding of this isolated problem. Numerical studies have proven crucial, as experiments of such interactions are extremely difficult to realize because of the need to measure pre- and post-shock turbulence states while controlling the shock front position. Since the pioneering work of Lee *et al.*,[21–23] the prescribed complexity of the interaction has incrementally increased, driven by the increase in available computational resources. Scale-resolving simulations of the canonical STI have not only improved our current fundamental understanding but have also informed modeling for practical engineering problems.[24–34]

Before addressing the key issues that characterize STI problems in the hypersonic regime, it is important to first define the canonical configuration. This requires a precise characterization of the turbulence properties ahead of the shock, as illustrated in Fig. 1. Specifically, the nature of the incoming turbulence must be described by its most critical parameters: turbulence intensity and characteristic lenght scale. The compressibility level of the turbulence, which plays a significant role in hypersonic STI, will be discussed later, while anisotropy effects will not be considered in this work.

In the canonical STI, where only upstream solenoidal disturbances are considered, the levels of the incoming turbulence fluctuations are characterized by the turbulent Mach number, $\mathcal{M}_t$, defined as

$$\mathcal{M}_t = \frac{\sqrt{R_{kk}}}{\tilde{c}} = \frac{\sqrt{2\,\mathrm{TKE}}}{\tilde{c}} = \sqrt{3}\frac{u_{\mathrm{rms}}}{\tilde{c}}, \tag{1}$$

where the quantities involved are the trace of the Reynolds stress tensor (R_{kk}), the Favre-averaged speed of sound ($\tilde{c}$), the turbulent kinetic energy (TKE), and the root mean square velocity fluctuations (u_{rms}). The higher the $\mathcal{M}_t$ for a given shock strength, the stronger the incoming fluctuations. In addition to $\mathcal{M}_t$, another dimensionless quantity is required to fully characterize the turbulence. This is typically the Taylor microscale Reynolds number, defined as

$$\mathrm{Re}_{\lambda_\alpha} = \frac{\overline{\rho} u_{\mathrm{rms}} \mathrm{L}_{\lambda_\alpha}}{\overline{\mu}}, \tag{2}$$

in terms of the time-averaged density, $\overline{\rho}$, and dynamic viscosity, $\overline{\mu}$, and the Taylor microscale

$$\mathrm{L}_{\lambda_\alpha} = \lambda_\alpha = \frac{\sqrt{\overline{u'^2_\alpha}}}{\sqrt{\overline{u'^2_{\alpha,\alpha}}}}, \tag{3}$$

where u'_α denotes velocity fluctuations in direction α. In this expression, Einstein notation is adopted, and $u'_{\alpha,\alpha}$ represents the derivative of velocity fluctuation u'_α with respect to the spatial direction α. Each flow direction can be associated with its own Taylor microscale and corresponding Reynolds number. In the case of isotropic turbulence considered here, this reduces to a single value, which is why the following discussion will only use singular references for it.

In accordance with every Reynolds number definition, the lower the Re_λ, the more viscous the flow. It is also possible to use an integral scale Reynolds number, Re_L (or Re_T) instead, which typically relies on the dissipation length scale, L_ϵ. The latter length scale also has different definitions throughout the literature but generally relates to R_{kk} (or TKE) and the dissipation rate of TKE, ϵ. The above two dimensionless numbers, $\mathcal{M}_t$ and $\mathrm{Re}_{\lambda_\alpha}$, are used to characterize the upstream turbulence when it is composed of solenoidal disturbances only. In addition, the shape of the turbulent kinetic energy spectrum, which provides information on how much kinetic energy is contained in eddies with a given wavenumber or length, should also be taken into account.

In terms of analysis, the three-dimensional flow problem is often reduced to one dimension by performing spatial and temporal averaging (in that order) at each streamwise planar location within the domain. Various flow statistics, including TKE, are analyzed, as discussed in Sec. III A. For TKE in particular, its evolution is best understood by examining its budget, which is derived from the trace of the Reynolds stress tensor transport equations, as outlined by Lee *et al.*[21]

The definition of the Reynolds' stress components is given in terms of the Favre average

$$R_{ij} = \widetilde{u''_i u''_j} = \frac{\overline{\rho u''_i u''_j}}{\overline{\rho}}. \tag{4}$$

The mechanisms underlying the amplification of Reynolds stress components and TKE are extensively

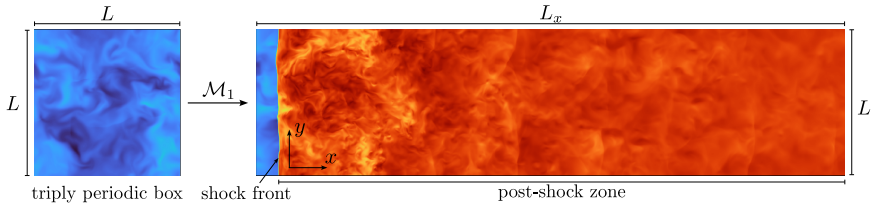

FIG. 1. Illustration of the canonical shock-turbulence interaction problem.

discussed in the literature (see, for example, 21, 22, 35–37). The energy spectrum tensor

$$\Phi_{ij} = \frac{1}{(2\pi)^2} \int R_{ij}(\mathbf{r})\, \mathrm{e}^{-\mathbf{k}\cdot\mathbf{r}} \mathrm{d}^3 r \tag{5}$$

is the Fourier transform of the velocity correlation tensor R_{ij}. The advantage of Fourier space is that it can be used to define the energy spectrum function, which under the isotropic assumption employed in this work, takes the form

$$E(k) = 2\pi k^2 \sum_i \Phi_{ii}(k). \tag{6}$$

When evaluating the interaction of the turbulence box with the shock plane (see Fig. 1), the relevant parameters include the shock strength—represented by the shock Mach number $\mathcal{M}_1 = u_1/c_1$—as well as the turbulence flow properties defined above. When the Mach number is sufficiently high, as in hypersonic flows where $\mathcal{M}_1 \geq 5$, turbulence compressibility effects can become significant, directly impacting the behavior and structure of the turbulence ahead of the shock. For sufficiently small turbulent fluctuations, compressible turbulence can be approximated as a linear superposition of three types of modes (or waves): acoustic (sound-wave), vorticity (also known as solenoidal), and entropy modes. This classification stems from Kovásznay's work,[38] which involved linearizing the Navier-Stokes equations in terms of small perturbations (with respect to the mean). The analysis revealed several linearly independent solutions, which were categorized into the three aforementioned categories. The interaction of any of these waves with a shock wave leads to the generation of all three modes through non-linear processes. The linear independence of these modes (in a first-order approximation for $\mathcal{M}_t \ll 1$) forms the basis of Linear Interaction Analysis (LIA), a technique first introduced by Ribner[39,40] and Moore,[41] and later extended by Chang[42] to account for entropy waves. Further details are provided in Sec. II.

LIA has become a useful tool in the analyses of canonical STI as it provides rapid estimations against which DNS or other numerical results can be compared. It can also be used in a predictive manner, but due to the underlying assumptions, its validity to the desired interaction (turbulence type and shock strength) must be carefully evaluated first. For instance, for isotropic turbulent flows, LIA finds that the TKE amplification factor does not depend on the shape of the spectrum $E(k)$, nor on $\mathrm{Re}_{\lambda_\alpha}$ or $\mathcal{M}_t$, the only independent parameters being the shock intensity $\mathcal{M}_1$ and the gas compressibility through the specific heat ratio γ. Also noteworthy is the adoption of Rapid Distortion Theory (RDT) to study the STI problem analytically;[43–45] however, its assumptions are even more restrictive than those of LIA.[37,46]

Turbulence compressibility is not the only factor that distinguishes STI in hypersonic flow conditions. High-temperature effects, such as vibrational excitation, molecular dissociation, and ionization, may also become significant as the Mach number and stagnation enthalpy exceed certain thresholds.[47] However, most canonical STI work to date has adopted constant heat capacities, i.e., a calorically perfect gas behavior, which may not be accurate when high-enthalpy effects, such as vibrational excitation or chemical non-equilibrium, become relevant. In a range of flight conditions, these effects may coexist with turbulent flows (see, e.g., Fig. 1 of Longo *et al.*[1]). As a result, it is also important to study, understand, and characterize the influence of non-equilibrium gas effects on the canonical STI.

When the turbulent Mach number is not sufficiently small, and/or the characteristic turbulence scales are comparable to the size of the thermochemical non-equilibrium region, the limitations of LIA hinder its applicability, making numerical simulations necessary. The limitations in LIA lead to a cut-off in the turbulence spectrum $E(k)$, where the effect of the smallest eddies (corresponding to the largest values of k) is not considered, as occurs in LIA applied to detonation-turbulence interaction.[48–50] In other words, for LIA to remain valid, variations in the upstream Mach number should be small compared to the mean incoming Mach number, and the residence time at the shock plus non-equilibrium region should be small compared to the turbulence time scale. In fact, detonation-turbulence interaction exhibits strong parallels to the shock-turbulence interaction problem, especially when relaxation times are of the same order. In such cases, DNS has proven effective in capturing the key turbulence properties in the post-shock reacting region. These studies reveal that turbulence accelerates the consumption of fuel and oxidizer by enhancing the production of intermediate radicals.[51–54] Similarly, the primary motivation of this work is to investigate the ul-

timate role of turbulence in hypersonic phenomena in air and, conversely, the impact of hypersonic effects on the post-shock turbulence field.

This study is inspired by the efforts of the NATO-STO AVT-352 working group on hypersonic turbulence. The group's contributions range from characterizing experimental hypersonic facilities to applying CFD to turbulence challenges. This work focuses on the fundamental physics of compressible turbulence in hypersonic conditions from a theoretical and numerical perspective. On the theoretical side, we employ a linear interaction analysis framework built on previous works.[47,55,56] This framework enables LIA for multi-component mixtures by using the Combustion Toolbox[57] to incorporate compressible and thermochemical effects. Theoretical (LIA) and numerical (DNS) results are presented across a wide range of Mach numbers to characterize the influence of upstream turbulence compressibility in the hypersonic regime.

The paper is structured as follows. Section II discusses the LIA developments that enable the study of canonical STI for both calorically perfect and imperfect gases. Section III focuses on CFD work, offering a comprehensive overview of DNS and LES studies related to canonical STI, along with recent advancements addressing hypersonic thermochemical non-equilibrium effects. Finally, the conclusions are presented in Sec. IV. This work aims to provide a comprehensive review of the canonical STI problem, serving as a foundation for further fundamental studies and explorations.

II. LINEAR INTERACTION ANALYSIS

The section is structured as follows. First, the concept of linear interaction analysis (LIA) is introduced in Sec. II A within the context of the canonical shock-turbulence interaction (STI) problem: an isotropic spectrum of velocity, density and pressure weak disturbances impacting on a planar shock wave. This includes the mathematical formulation and quantities of interest for such studies. This is followed by Sec. II B, which examines LIA developments specifically adapted to hypersonic regimes.

A. LIA in canonical STI

1. Mathematical Formulation

To characterize the interaction of a shock wave with incoming turbulence, it is necessary to first consider the nature of the turbulent disturbances approaching the shock. Following Kovásznay's decomposition,[38] these disturbances can be categorized into three fundamental types: vortical, entropic, and acoustic fluctuations. Each type of upstream fluctuation generates a distinct set of post-shock vortical, entropic, and acoustic perturbation eigenmodes. To examine how these disturbances interact with and are affected by the shock, we employ the LIA formalism introduced by Ribner[39,40] and Moore.[41] LIA decomposes the weak turbulent field ahead of the shock into a Fourier superposition of statistically independent, infinitesimally small, single-mode shear waves. For the sake of clarity, this subsection focuses initially on the vortical disturbance case, as it has been extensively studied and provides a straightforward introduction to the problem. The analysis closely follows the approach outlined in Huete *et al.*[47]

Hereafter, we define a Cartesian coordinate system where the unperturbed shock lies in the $(y',\, z')$ plane, and the x'-axis aligns with the mean streamwise direction of the incoming flow. If the pre-shock turbulence is isotropic, there is no preferred direction for the wavenumber vector $\mathbf{k}$, so the amplitude of the vorticity modes depends solely on $k = |\mathbf{k}|$. Likewise, there is no favored orientation of the wavenumber vector relative to the shock surface. In principle, this would require a three-dimensional formulation to describe the interaction. But by simply rotating the reference frame, the problem can be reduced to two-dimensions. Thus, for an incident wavenumber vector oriented arbitrarily in space, defined by the latitude and longitude angles θ and φ, the reference frame can be rotated counterclockwise around the x'-axis by an angle ψ, corresponding to the longitudinal inclination of the incident wave, as shown in Fig. 2. Use of the new reference frame $(x,\, y,\, z)$ reduces the interaction problem to two dimensions, eliminating all variations with respect to z.

After the aforementioned rotation, the wavenumber-vector components in the streamwise and transverse directions are

$$k_x = k\cos\theta, \quad k_y = k\sin\theta, \tag{7}$$

respectively, with $k_z = 0$ by construction. Similarly, in the laboratory reference frame, the vorticity vector of the incident wave in the pre-shock gas can be expressed as

$$\boldsymbol{\omega_1} = (\delta\boldsymbol{\omega_1})\mathrm{e}^{\mathrm{i}(k_x x + k_y y)}, \tag{8}$$

with

$$\delta\omega_{x,1} = -\varepsilon k\langle c_2\rangle \sin\theta\cos\varphi, \tag{9a}$$
$$\delta\omega_{y,1} = \ \ \varepsilon k\langle c_2\rangle \cos\theta\cos\varphi, \tag{9b}$$
$$\delta\omega_{z,1} = -\varepsilon k\langle c_2\rangle \sin\varphi, \tag{9c}$$

being the vorticity amplitude in each direction. In this formulation, $\langle c_2\rangle$ denotes the mean speed of sound in the post-shock gas, and ε is a dimensionless velocity fluctuation amplitude, which is small in the linear theory, $\varepsilon \ll 1$.

The vorticity of the incident wave engenders a fluctuating velocity field in the pre-shock gas given by

$$\mathbf{v_1} = (\delta\mathbf{v_1})\mathrm{e}^{\mathrm{i}(k_x x + k_y y)}, \tag{10}$$

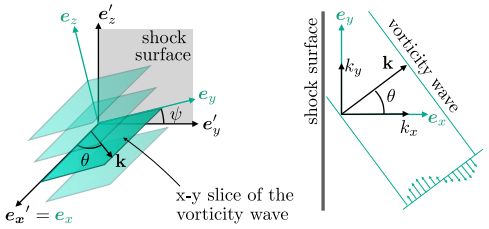

FIG. 2. Simplification of a three-dimensional problem of a shock interacting with an arbitrarily oriented vorticity wave to a two-dimensional problem by rotating the reference frame around the streamwise axis. Reproduced from C. Huete, A. Cuadra, M. Vera, and J. Urzay. Phys. Fluids **33**, 086111 (2021), with the permission of AIP Publishing.

whose amplitude is

$$\delta u_1 = \varepsilon\langle c_2\rangle \sin\theta \sin\varphi, \tag{11a}$$
$$\delta v_1 = -\varepsilon\langle c_2\rangle \cos\theta \sin\varphi, \tag{11b}$$
$$\delta w_1 = \varepsilon\langle c_2\rangle \cos\varphi \tag{11c}$$

in the x, y, and z directions, respectively. Specifically, the z-component of the fluctuation velocity vector is uniform along z. This component will not be considered further in the analysis, as it passes through the shock unaltered due to the conservation of tangential momentum. Additionally, note that (8) and (10) are related by the definition of vorticity, $\boldsymbol{\omega_1} = \mathbf{k}\times\mathbf{v_1}$. Moreover, the velocity field given by (10)–(11) satisfies the incompressibility condition, $\mathbf{k}\cdot\mathbf{v_1} = 0$. Lastly, implicit in the definitions given above is that the incident vorticity wave is inviscid, or equivalently, that the pre-shock Reynolds number of the fluctuation, $2\pi|\mathbf{v}_1|/(k\nu_1)$, is infinitely large.

To illustrate the analysis, a particular form of the pre-shock vorticity fluctuation corresponding to the inviscid Taylor-Green vortex

$$\omega_{z,1}(x,y) = \varepsilon_r\langle c_2\rangle \left(\frac{k^2}{k_y}\right)\cos(k_x x)\sin(k_y y) \tag{12}$$

is employed in the numerical results presented below, with $\omega_{x,1} = \omega_{y,1} = 0$. The corresponding streamwise and transverse components of the velocity fluctuations in the pre-shock gas are given by

$$u_1(x,y) = \varepsilon_r\langle c_2\rangle \cos(k_x x)\cos(k_y y), \tag{13a}$$
$$v_1(x,y) = \varepsilon_r\langle c_2\rangle \left(\frac{k_x}{k_y}\right)\sin(k_x x)\sin(k_y y), \tag{13b}$$

respectively. In this formulation, ε_r is the amplitude of the pre-shock streamwise velocity fluctuations

$$\varepsilon_r = \varepsilon\sin\theta\sin\varphi, \tag{14}$$

with $\varepsilon_r \ll 1$ in the linear theory. In this linear theory, the vorticity and the streamwise and transverse velocity components in the post-shock gas reference frame are expanded to first order in ε_r as

$$\omega = \varepsilon_r k_y\langle c_2^2\rangle\hat{\omega}, \quad u = \varepsilon_r\langle c_2\rangle\hat{u}, \quad v = \varepsilon_r\langle c_2\rangle\hat{v}, \tag{15}$$

respectively, with $\hat{\omega}$, $\hat{u}$, and $\hat{v}$ being the corresponding dimensionless fluctuations. The post-shock pressure and density can be similarly expressed as

$$P = \langle P_2\rangle + \varepsilon_r\langle\rho_2\rangle\langle c_2\rangle^2\hat{p}, \quad \rho = \langle\rho_2\rangle(1+\varepsilon_r\hat{\rho}), \tag{16}$$

with $\hat{p}$ and $\hat{\rho}$ being the dimensionless fluctuations of pressure and density, respectively. Angle brackets indicate time-averaged quantities associated with perturbation-free shock jump conditions. In this way, all fluctuations are defined to have a zero-time average. Assuming that the Reynolds number of the post-shock fluctuations is infinitely large, expansions (15)–(16) can be used to express the linearized Euler conservation equations, which can be combined into a single two-dimensional periodically symmetric wave equation for the post-shock pressure fluctuations. If the transient evolution is sought, this sound-wave equation is integrated within the spatio-temporal domain bounded by the leading reflected sonic wave traveling upstream and the shock front moving downstream. For the long-time asymptotic evolution, the analysis can be simplified to that of obtaining the amplitudes of the different modes through the normal mode analysis, which necessitates from the distorted shock boundary condition.

The boundary condition at the shock front is obtained from the linearized Rankine-Hugoniot jump conditions assuming that the displacement of the shock $\xi_s = \xi_s(y,t)$ from its average flat shape is much smaller than k_y^{-1}. In this limit, at any transverse coordinate, the Rayleigh-Hugoniot jump conditions can be applied at the mean shock front location, and can be linearized about the mean thermochemical-equilibrium post-shock gas state, namely $\mathcal{R} = \rho_2/\rho_1$, $\mathcal{P} = P_2/P_1$, and $\mathcal{M}_2 = u_2/c_2$, given by

$$\mathcal{R} = \frac{(\gamma+1)\mathcal{M}_1^2+\gamma-1}{(\gamma-1)\mathcal{M}_1^2+2}, \quad \mathcal{P} = \frac{2\gamma\mathcal{M}_1^2-\gamma+1}{\gamma+1}, \tag{17}$$

and $\mathcal{M}_2 = \mathcal{M}_1/\sqrt{\mathcal{R}\mathcal{P}}$ for an ideal gas EoS in thermochemical equilibrium. Additionally, the inverse of the slope of the Hugoniot curve normalized with the slope of the Rayleigh line

$$\Gamma = -\left(\frac{P_2-P_1}{1/\rho_1-1/\rho_2}\right)\frac{\mathrm{d}(1/\rho_2)}{\mathrm{d}P_2} = \gamma\frac{\mathcal{M}_1^2}{\mathcal{R}^2}\left(\frac{\partial\mathcal{P}}{\partial\mathcal{R}}\right)^{-1} \tag{18}$$

takes the form $\Gamma = \mathcal{M}_1^{-2}$ for an ideal gas in thermochemical equilibrium. These expressions can be used to write

the linearized RH equations as follows:

$$\frac{\partial\hat{\xi}_s}{\partial\tau} = \frac{\mathcal{R}\,(1-\Gamma)}{2\mathcal{M}_2\,(\mathcal{R}-1)}\hat{p}_s - \hat{u}_1, \tag{19a}$$

$$\hat{u}_s = \frac{1+\Gamma}{2\mathcal{M}_2}\hat{p}_s + \hat{u}_1, \tag{19b}$$

$$\hat{v}_s = \hat{v}_1 - \mathcal{M}_2\,(\mathcal{R}-1)\,\frac{\partial\hat{\xi}_s}{\partial\hat{y}}, \tag{19c}$$

$$\hat{\rho}_s = \frac{\Gamma}{\mathcal{M}_2^2}\hat{p}_s, \tag{19d}$$

where τ is the dimensionless time coordinate and (19c) corresponds to the conservation of tangential velocity. In (19), the function $\hat{\xi}_s = k_y\xi_s/\varepsilon_r$ represents the dimensionless shock displacement, whereas $\hat{p}_s$, $\hat{\rho}_s$, $\hat{u}_s$, and $\hat{v}_s$ are, respectively, the dimensionless fluctuations of pressure, density, streamwise velocity and transverse velocity immediately downstream of the shock front.

In a reference frame that moves with the shock front immediately downstream the perturbed shock surface (denoted by subscript 2), a corresponding set of perturbations is generated. For the velocity components and pressure, these downstream perturbations are evaluated as

$$\hat{u}_{2s}(\tau) = \frac{\delta u_{2s}}{\varepsilon_r c_2} = (\mathcal{U}_r + \mathcal{U}_a)\cos(\omega_s^r\tau + \phi), \tag{20a}$$

$$\hat{v}_{2s}(\tau) = \frac{\delta v_{2s}}{\varepsilon_r c_2} = (\mathcal{V}_r + \mathcal{V}_a)\sin(\omega_s^r\tau), \tag{20b}$$

$$\hat{p}_{2s}(\tau) = \frac{\delta P_{2s}}{\varepsilon_r\rho_2 c_2^2} = \mathcal{P}\sin(\omega_s^r\tau), \tag{20c}$$

with $\omega_s^r = \mathcal{R}\mathcal{M}_2/\tan\theta$. The amplitudes of the post-shock modes $\mathcal{U}_r(\theta)$, $\mathcal{U}_a(\theta)$, $\mathcal{V}_r(\theta)$, $\mathcal{V}_a(\theta)$, and $\mathcal{P}(\theta)$ are unknown functions of θ to be determined with the aid of the shock boundary condition and the isolated-shock assumption. In this work, the far-field amplitudes are computed in the asymptotic limit $\mathcal{M}_2\tau \gg 1$ and sufficiently far from the shock, as discussed in Ref. 47. Note that in (20), the transverse coordinate dependence is omitted, $\sim\cos(k_y y)$ for the longitudinal and $\sim\sin(k_y y)$ for the transverse velocity field, as it is not affected by the shock passage in the linear regime where the transverse periodicity is not broken. To distinguish between the different contributions, the subscripts r, a refer to the nature of the perturbation: rotational or acoustic.

2. Turbulent Kinetic Energy amplification factor

The weak isotropic turbulence in the pre-shock gas can be modeled as a linear superposition of incident vorticity waves, with amplitudes ε that vary according to the wavenumber, consistent with an isotropic energy spectrum $E(k) = \varepsilon^2(k)$. The root mean square (rms) of the velocity and vorticity fluctuations in the pre-shock gas can be derived by applying the assumption of isotropy. This assumption states that the probability of an incident wave having orientation angles between θ and $\theta+d\theta$, and between φ and $\varphi + d\varphi$, is proportional to the solid angle element $\sin\theta\,\mathrm{d}\theta\,\mathrm{d}\varphi/(4\pi)$. This leads to the following expressions:

$$\frac{\langle u_1'^2\rangle}{\varepsilon^2\langle c_2\rangle^2} = \frac{1}{3}, \quad \frac{\langle v_1'^2\rangle}{\varepsilon^2\langle c_2\rangle^2} = \frac{1}{6}, \quad \frac{\langle w_1'^2\rangle}{\varepsilon^2\langle c_2\rangle^2} = \frac{1}{2} \tag{21}$$

for the pre-shock rms velocity fluctuations. The TKE amplification factor across the shock wave is defined as

$$K = \frac{\langle u_2'^2\rangle + \langle v_2'^2\rangle + \langle w_2'^2\rangle}{\langle u_1'^2\rangle + \langle v_1'^2\rangle + \langle w_1'^2\rangle} = \frac{\langle u_2'^2\rangle + \langle v_2'^2\rangle}{\varepsilon^2\langle c_2\rangle^2} + \frac{1}{2} \tag{22}$$

$$= \frac{1}{2}\left[\int_0^{\pi/2}\left(\hat{u}^2 + \hat{v}^2\right)\sin^3\theta\mathrm{d}\theta + 1\right], \tag{23}$$

where use of (21) has been made. Furthermore, K can also be decomposed linearly into acoustic and vortical modes as $K = K_a + K_r$, with

$$K_a = \frac{1}{3}\int_1^\infty\left(\mathcal{U}_a^2 + \mathcal{V}_a^2\right)\mathrm{P}(\zeta)\mathrm{d}\zeta = \frac{1}{3}\int_1^\infty \Pi_s^2\mathrm{P}(\zeta)\mathrm{d}\zeta,$$
$$K_r = \frac{1}{2} + \frac{1}{3}\int_0^\infty\left(\mathcal{U}_r^2 + \mathcal{V}_r^2\right)\mathrm{P}(\zeta)\mathrm{d}\zeta. \tag{24}$$

The entropic mode does not contain any kinetic energy, since entropy fluctuations are decoupled from velocity fluctuations in the inviscid linear limit. In equation (24), $\mathrm{P}(\zeta)$ is a probability-density distribution given by

$$\mathrm{P}(\zeta) = \frac{3}{2}\frac{\mathcal{M}_2^4\mathcal{R}^4\sqrt{1-\mathcal{M}_2^2}}{\left[\mathcal{M}_2^2\mathcal{R}^2 + \zeta^2\,(1-\mathcal{M}_2^2)\right]^{5/2}}, \tag{25}$$

which satisfies the normalization condition $\int_0^\infty \mathrm{P}(\zeta)\mathrm{d}\zeta = 1$. Additionally, the velocity amplitudes $\mathcal{U}_a$, $\mathcal{U}_r$, $\mathcal{V}_a$, and $\mathcal{V}_r$ are obtained using the long-time far-field asymptotic expressions. The lower integration limit of K^a is $\zeta = 1$ because the acoustic mode decays exponentially with distance downstream of the shock in the long-wave regime $\zeta < 1$. However, such decaying contribution needs to be added to K^a, and therefore to K, when evaluating the solution in the near field.

B. LIA in hypersonic STI

1. Some prior considerations of hypersonic shocks

Hypersonic flows are influenced by the rates governing internal energy relaxation and chemical reactions. The relatively slow relaxation of a gas vibrational modes can interact with the gas dynamics in several ways. Most notably, the vibrational modes absorb energy and alter the post-shock conditions when they are active. Additionally, the vibrational state of the gas significantly affects its dissociation rate.[58] Even if dissociation is not crucial, as can often be the case in the hypersonic regime, the

relaxation time $t_{\rm vib}$ of the vibrational modes is used to define the thickness of the relaxation layer $\delta_{\rm vib} \sim u_2\, t_{\rm vib}$. In STI, there always exits a post-shock relaxation region where turbulence is dissipated by viscous effects, with a characteristic thickness δ_ν. These two relaxation layers must be compared to determine the characteristic vibrational Damköhler number: ${\rm Da} = \delta_\nu/\delta_{\rm vib} = \delta_\nu/(u_2\, t_{\rm vib})$. For shock waves with $\mathcal{M}_1 \geq 5$, thermochemical non-equilibrium arises in the post-shock region, where preferential excitation of rotational and translational energy modes gives rise to finite-rate relaxation of the vibrational-electronic energy modes. Energy exchange between these non-equilibrium internal degrees of freedom and the rotational-translational modes proves crucial not only for predicting heat fluxes but also for the evaluation of chemical production rates, with the effective vibrational excitation modulating the reaction rates through vibration-dissociation coupling.[59] For finite-rate thermochemical relaxation that proceeds on the advective timescale, namely ${\rm Da} \simeq 1$, direct numerical solution of the relevant non-linear conservation laws generally proves necessary for characterizing the non-equilibrium flow physics[60–62].

The canonical non-hypersonic STI, for which the upstream turbulence remains isotropic, can be simply formulated in terms of the dominant dimensionless parameters alone. In particular, according to LIA, the TKE amplification factor K depends on the type of gas, as characterized by its adiabatic coefficient ($\gamma \simeq 1.4$ for air), and shock strength, typically through the upstream Mach number, $\mathcal{M}_1$. More realistic conditions can be studied through numerical simulations, which introduce two additional dimensionless numbers: turbulent intensity (through the turbulent Mach number, $\mathcal{M}_t$) and the Taylor microscale Reynolds number, ${\rm Re}_\lambda$. Efforts have been made to consolidate and simplify the parametric dependencies. For instance, Donzis[63,64] defined a novel parameter $\mathcal{K} = \mathcal{M}_t/[{\rm Re}_\lambda^{1/2}(\mathcal{M}_1 - 1)]$ based on similarity arguments related to the instantaneous shock thickness. This parameter represents the ratio of the Kolmogorov length scale to the laminar shock thickness and effectively collapses all available data regarding the streamwise component of the TKE amplification factor.[37] In the strong-shock limit, this parametric collapse relies in the concept of classical dimensional similarity through the so-called hypersonic similitude. Consequently, the TKE amplification factor approaches a constant value as the shock Mach number increases indefinitely.

At low-hypersonic flight speeds, the calorically-perfect description, in which the gas is treated as having a constant specific heat ratio, γ, can often suffice, with two perfect gases sharing similar values of γ exhibiting physical similarity. At the hypersonic frontier, the equation of state (EoS) for an ideal gas almost universally remains applicable; however, even for modest Mach numbers, air becomes thermally rather than calorically perfect, meaning that γ is at least a function of temperature $\gamma(T)$. Thus, by simple dimensional analysis, we can conclude that the strong temperature dependence exhibited by some of these phenomena precludes the reduction of the problem by using parameter $\mathcal{K}$ alone in the hypersonic flow regime. Depending on the relevant flow-field conditions, to include the freestream pressure, chemical composition, and Mach number, the characteristic vibrational Damköhler number can vary significantly. For large-scale turbulence, with $\delta_{\rm vib} \ll \delta_\nu$, the separation of scales allows the vibrational relaxation layer to be considered infinitesimally thin. Consequently, the specific heat ratio can be evaluated using the equilibrium post-shock state, $\gamma(T_2) = $ constant, before viscous dissipation occurs. This situation corresponds to ${\rm Da} \to \infty$. When $\delta_{\rm vib}$ is of the order of δ_ν, the specific heat ratio immediately behind the shock is determined by upstream conditions, $\gamma(T_1)$, and its evolution towards $\gamma(T_2)$ roughly coincides with the process of viscous dissipation, so thermochemical non-equilibrium phenomena must be solved along the post-shock turbulence decay, with the two processes being coupled. In the opposite limit, where $\delta_{\rm vib} \gg \delta_\nu$, the ratio of specific heats remains constant at $\gamma = \gamma(T_1)$ throughout the entire viscous dissipation process. This scenario corresponds to ${\rm Da} \to 0$. Note that further effects associated with dissociation and ionization are characterized by different (chemical) Damköhler numbers, with similar limiting behavior arising in these phenomena.

2. The Rankine-Hugoniot curve in hypersonics

The simplest method to evaluate the deviation from the calorically perfect assumption involves considering the characteristic vibrational temperature of the molecules. For example, for air in thermal equilibrium, the specific internal energy behind the shock can be described as

$$e_2 = c_v T_2\,[1 + f_v(T_2)] = \frac{1}{\gamma - 1}\frac{P_2}{\rho_2}\,[1 + f_v(T_2)]\,, \quad (26)$$

where the auxiliary function f_v accounts for the energy stored in the molecules in form of vibrational modes. In the harmonic-oscillator model, which works well sufficiently far from dissociation, the auxiliary functions reads

$$f_v(T_2) = \frac{\gamma - 1}{Y_{\rm O_2} + \mathcal{W}\,(1 - Y_{\rm O_2})}\left[Y_{\rm O_2}\frac{\Theta_{\rm O_2}/T_2}{{\rm e}^{\Theta_{\rm O_2}/T_2} - 1} + \mathcal{W}\,(1 - Y_{\rm O_2})\,\frac{\Theta_{\rm N_2}/T_2}{{\rm e}^{\Theta_{\rm N_2}/T_2} - 1}\right], \quad (27)$$

where $\mathcal{W} = W_{\rm O_2}/W_{\rm N_2} = 32/28 = 8/7$ is the ratio of molecular weights of molecular oxygen to molecular nitrogen, and $\Theta_{\rm O_2} = 2270$ K and $\Theta_{\rm N_2} = 3390$ K are the corresponding vibrational temperatures, respectively. In the case of air, the mass fraction of oxygen is $Y_{\rm O_2} = 0.2315$, and the diatomic adiabatic index is $\gamma = 7/5$. Note that $f_v \to 0$ as $T_2/\Theta_v \to 0$. Ahead of

the shock, where the gas is presumed to be cold (meaning sufficiently cold to neglect vibrational effects), i.e., $T_1 \ll \Theta_v$, the equation for the specific internal energy reduces to $e_1 = (5/2)R_g T_1$, whereas in the post-shock gas, where $T_2 \sim \mathcal{M}_1^2 T_1$, the specific internal energy e_2 requires consideration of translational, rotational, and vibrational degrees of freedom.

The advantage of (26) is that it enables evaluating the relative importance of vibrational effects by simply comparing the corresponding temperature with the value of Θ_v. This facilitates discussions grounded in fundamental properties. However, the equation assumes a perfect harmonic oscillator model for the molecular vibrations, which becomes less accurate as vibrations intensify and approach the dissociation threshold. For air, which is predominantly composed of O_2 and N_2, the generalization of the analysis is straightforward, with molecular oxygen being the first to exhibit non-negligible vibrational effects.

Although this complicates the physical discussion, for the quantitative study of these phenomena it is convenient to introduce the NASA polynomials to evaluate $c_p(T)$, and consequently $e(T) = [c_p(T) - R_g]\,T$, along with the corresponding specific heat ratio $\gamma(T) = c_p(T)/[c_p(T) - R_g]$, to compute the Rankine-Hugoniot equations for thermally perfect gases. This approach offers significant advantages: i) the range of validity is higher, and ii) most numerical codes used in combustion processes already incorporate NASA polynomials. In particular, the results presented in this work make use of the NASA 9-coefficient polynomials database,[65] which ranges up to 20 000 K.

As previously discussed, for Mach numbers significantly exceeding 5, dissociation and/or ionization effects must be included in the analysis. To evaluate their relative importance in the thermochemical equilibrium flow, an illustrative example is provided in Fig. 3(a), where the Hugoniot curve ($\mathcal{P} = P_2/P_1$ vs. $1/\mathcal{R} = \rho_1/\rho_2$) is plotted for normal shocks in air with pre-shock conditions: $T_1 = 300$ K, $P_1 = 1$ atm, and volume % composition $\{N_2, O_2\} = \{79, 21\}$. Full equilibrium calculations have been carried out with the Combustion Toolbox[57,66,67] assuming a 26-species mixture using NASA 9-coefficient polynomials. The thermochemical equilibrium results are compared with the analytical solution obtained for a thermochemically frozen gas with constant composition. It is seen that, due to the endothermicity of the dissociation processes, a significantly higher compression ratio is achieved compared to that in the thermochemically frozen case. Figure 3 (b, left y-axis) shows the temperature jump $\mathcal{T} = T_2/T_1$ vs. upstream Mach number $\mathcal{M}_1 = u_1/c_1$ for the same conditions. Both panels exhibit a similar behavior, with both the post-shock specific volume and temperature jump decreasing significantly below their frozen flow values because of the further increase in density and decrease in velocity. This trend finishes after a clear turning point associated with the change in the mean molecular structure. At some degree of dissociation, endothermic effects associated with bond-breaking are no longer dominant, and the balance of diatomic molecules vs. monoatomic species shifts to the latter. As the flow conditions continue to intensify, ionization processes play an increasingly significant role, leading to the production of ionized species and further modifying the thermodynamic state through additional energy absorption. If ionization is neglected, the theoret-

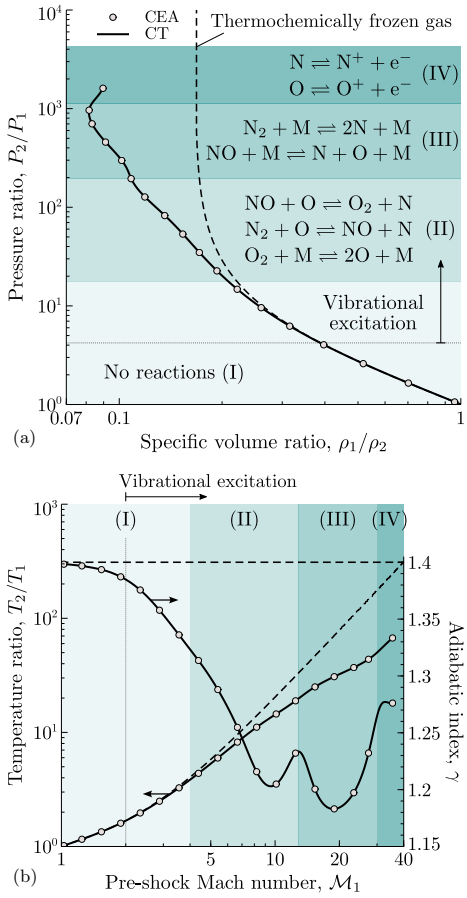

FIG. 3. Log-log RH curve (a), log-log temperature jump (b, left y-axis), and linear-log adiabatic index (b, right y-axis), as a function of the downstream Mach number for normal shocks propagating in air at $T_1 = 300$ K and $P_1 = 1$ atm; solid line: Combustion Toolbox (CT);[57,66,67] dashed line: thermochemical frozen gas approximation; circles: results by CEA code;[68] Roman numerals: regions with the dominant reactions labeled.

ical maximum compression ratio, $d+1$, decreases from 6 to 4, with d standing for the degrees of freedom of the species involved ($d=5$ for rigid diatomic molecules and $d=3$ for single atoms). Examining the adiabatic index γ in Fig.3 (b, right y-axis), we can clearly observe the effect of vibrational excitation, which leads to a lower adiabatic index due to the increased degrees of freedom. As the shock intensity—and consequently, the temperature—rises sufficiently to dissociate molecular oxygen, the adiabatic index increases due to the growing presence of monatomic oxygen (lower degrees of freedom). This pattern repeats with the vibrational excitation of molecular nitrogen, which lowers γ, followed by its subsequent dissociation into monatomic species. Additionally, ionization becomes a significant factor for $\mathcal{M}_1 \geq 30$. The roman numerals have been used in Fig. 3 to identify the dominant reactions in the different Mach regimes, starting with oxygen dissociation (region II), followed by nitrogen dissociation (region III), whose dissociation temperature is roughly twice that of oxygen, and finishing with their first ionization (region IV). Results have been compared with NASA's Chemical Equilibrium with Applications (CEA) code,[68] showing always an excellent agreement.

The resolution of the STI problem in the hypersonic regime follows the same steps outlined in the previous section. However, now the upstream gas is influenced by more than just vorticity disturbances. Instead, the shock is perturbed due to a combination of velocity (both rotational and acoustic), density (entropic and acoustic), and pressure (acoustic) disturbances. This leads to the following set of linearized Rankine-Hugoniot equations[56]

$$\frac{\mathrm{d}\hat{\xi}_s}{\mathrm{d}\tau} = \frac{\mathcal{R}\left(1-\Gamma\right)}{2\mathcal{M}_2\left(\mathcal{R}-1\right)}\hat{p}_{2s} - \frac{\mathcal{M}_2\mathcal{R}^2\left(1-2\mathcal{R}^{-1}-\Gamma_\rho\right)}{2\left(\mathcal{R}-1\right)}\hat{\rho}_{1s} + \frac{1}{\beta}\hat{u}_{1s} - \frac{1-\Gamma_p}{2\beta^2\mathcal{M}_2(\mathcal{R}-1)}\hat{p}_{1s}, \tag{28a}$$

$$\hat{u}_{2s} = \frac{1+\Gamma}{2\mathcal{M}_2}\hat{p}_{2s} - \frac{\mathcal{M}_2\mathcal{R}\left(1+\Gamma_\rho\right)}{2}\hat{\rho}_{1s} + \frac{1}{\beta}\hat{u}_{1s} - \frac{1+\Gamma_p}{2\beta^2\mathcal{M}_2\mathcal{R}}\hat{p}_{1s}, \tag{28b}$$

$$\hat{v}_{2s} = \frac{1}{\beta}\hat{v}_{1s} - \mathcal{M}_2\left(\mathcal{R}-1\right)\frac{\partial\hat{\xi}_s}{\partial\hat{y}}, \tag{28c}$$

$$\hat{\rho}_{2s} = \frac{\Gamma}{\mathcal{M}_2^2}\hat{p}_{2s} - \mathcal{R}\Gamma_\rho\hat{\rho}_{1s} - \frac{\Gamma_p}{\beta^2\mathcal{M}_2^2\mathcal{R}}\hat{p}_{1s}, \tag{28d}$$

where the following normalized RH-slope parameters are conveniently introduced

$$\Gamma = u_2^2\left.\frac{\partial\rho_2}{\partial P_2}\right|_{P_1,\rho_1} \text{ as in (18), and the additional factors}$$
$$\Gamma_\rho = \frac{\Gamma}{u_1^2}\left.\frac{\partial P_2}{\partial\rho_1}\right|_{P_1,\rho_2},\ \Gamma_p = \Gamma\left.\frac{\partial P_2}{\partial P_1}\right|_{\rho_1,\rho_2}. \tag{29}$$

For example, for an ideal gas that is calorically perfect and is in chemical equilibrium, $\Gamma = \mathcal{M}_1^{-2}$, as commented right after (18). The other two parameters reduce to $\Gamma_\rho = -\mathcal{R}^{-1}$ and $\Gamma_p = \mathcal{P}\mathcal{M}_1^{-2}$ in such conditions. As shown in Fig. 4 (a), the value of Γ becomes positive along the upper branch of the Hugoniot curve beyond the turning point $\Gamma = 0$. Along this branch, an increase in post-shock pressure induces a decrease in post-shock density. The role of Γ, Γ_ρ, and Γ_p in the description of the shock-turbulence interaction problem will be discussed in next section. These parameters can also be conveniently computed using the Combustion Toolbox.[57,66,67]

When evaluating (28), it is readily seen that as the shock strength increases, the ratio $1/\beta = c_1/c_2$ decreases inversely with $\mathcal{M}_1$, diminishing the significance of upstream velocity and pressure perturbations relative to the shock wave. In simpler terms, as the shock speed and post-shock variables grow unbounded with increasing Mach number, the density jump is the only one that remains finite. Consequently, only density disturbances, whether acoustic or entropic in nature, can substantially affect the shock as $\mathcal{M}_1 \to \infty$. However, since the Mach number is finite, the relative significance of different types of upstream perturbations also depends on their respective orders of magnitude. In the case of interest, where pressure disturbances in the upstream flow are expected to be very low and $c_1^2/c_2^2 \ll 1$, they can be safely neglected, and the focus shifts to density perturbations. Thus, it is relatively easy to see that, for upstream density disturbances to be non-negligible in STI, the following condition must be met

$$\frac{\delta\rho_1}{\rho_1} \sim \frac{c_1}{c_2}\frac{2}{\mathcal{M}_2\mathcal{R}\left(1+\Gamma_\rho\right)}\frac{\delta u_1}{c_1}. \tag{30}$$

For a calorically perfect gas with $\gamma = 1.4$ and $\mathcal{M}_1 = 5$, we find that $\delta\rho_1/\rho_1$ is non-negligible during shock passage when it is approximately one order of magnitude smaller than $\delta u_1/c_1$. As the shock intensity increases, the threshold for non-negligible density perturbations decreases. This conclusion is readily drawn by inspecting Fig. 4(b), which illustrates the influence of the prefactors A_ρ, A_u, and A_p derived from the upstream fluctuation terms in (28b), namely

$$\hat{u}_{2s} = \frac{1+\Gamma}{2\mathcal{M}_2}\hat{p}_{2s} - A_\rho\hat{\rho}_{1s} + A_u\hat{u}_{1s} - A_p\hat{p}_{1s}, \tag{31}$$

as a function of the incident Mach number. These prefactors quantify the respective contributions of upstream density, velocity, and pressure fluctuations, providing insights into the increasing role of density perturbations as the Mach number grows.

Note that, although the role of upstream density disturbances in STI has been addressed in the literature—primarily to emulate the interaction of oblique shocks with turbulent high-speed boundary layers—the key takeaway is that in hypersonic conditions, upstream density disturbances must always be carefully evaluated. Otherwise, the canonical prescription of STI may be inaccurate. It should be noted that density disturbances

ahead of the shock may also arise due to numerical turbulence forcing mechanisms.[69] Therefore, any comprehensive attempt to adequately address STI should take these disturbances into account.

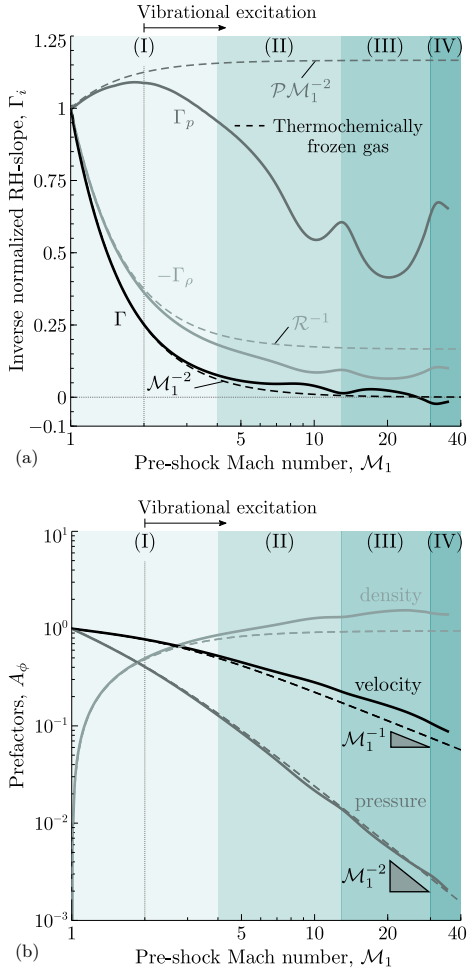

FIG. 4. Linear-log RH-slope parameters (a) and log-log influence of the upstream fluctuations on the downstream velocity perturbation [see Eqs. (28b) and (31)](b) as a function of the upstream Mach number for normal shocks propagating in air at $T_1 = 300$ K and $P_1 = 1$ atm. Solid lines: calorically imperfect gas; Dashed lines: calorically perfect gas; Roman numerals: regions with the dominant reactions labeled in Fig. 3.

3. *Influence of the nature of the upstream turbulence*

a. Vortical fluctuations In addition to the standard assumptions of LIA applied previously in canonical STI—specifically, that velocity perturbations are much smaller than the corresponding speed of sound—the incorporation of thermochemical effects requires that the characteristic size of shock wrinkles be significantly larger than the thickness of the thermochemical nonequilibrium region behind the shock. The accuracy of this approximation in practical hypersonic systems is expected to improve with increasing flight Mach numbers and decreasing flight altitudes, as will be discussed in Sec. II C. This is because the temperature behind the shock increases with the Mach number, while the upstream density increases at lower altitudes, which in turn enhances intermolecular collisions and facilitates the rapid achievement of thermochemical equilibrium. Unlike Ref. 47, which examined single-species symmetric diatomic gases, the RH curve in this study is not expressed analytically in terms of fundamental parameters like rotational, vibrational, or dissociation characteristic temperatures. However, the current approach incorporates additional complexities, such as recombination into multi-species gases and ionization.

As before, the weak isotropic turbulence in the pre-shock gas can be represented by a linear superposition of incident vorticity waves whose amplitudes ε vary with the wavenumber in accordance with an isotropic energy spectrum $E(k) = \varepsilon^2(k)$. The root mean square of the velocity and vorticity fluctuations in the pre-shock gas can be calculated by invoking the isotropy assumption. The TKE amplification factor across the shock wave is of utmost interest in the interaction of shock waves with turbulence. By performing the theoretical analysis described in Huete *et al.*,[47] with the details omitted here for brevity, the value of K can be expressed as an integral formula—corresponding to an isentropically weighted sum of contributions of the vorticity perturbations impinging on the planar shock—that ultimately depends on the post-shock properties: mass compression ratio ρ_2/ρ_1, post-shock Mach number $\mathcal{M}_2$, and a non-dimensional parameter that accounts for the RH-slope Γ, which are again computed with the aid of the Combustion Toolbox.[57,66,67] In our case, we have a multi-species mixture of gases composed mainly of O_2 and N_2, which have different characteristic dissociation temperatures.

The resulting curve for K as a function of the pre-shock Mach number $\mathcal{M}_1$ (solid black line) is shown in Fig. 5. The curve exhibits two distinguished peaks corresponding to regions (II) and (III) of Fig. 3. The non-monotonicity of K is dictated by the behavior of the vorticity generation across the shock, since acoustic turbulent kinetic energy is negligible in hypersonic conditions. This effect, not shown explicitly in this work, was analyzed in detail in Huete *et al.*[47] Two main effects are found to govern the post-shock perturbation flow: the mass compression ratio, whose amplification via en-

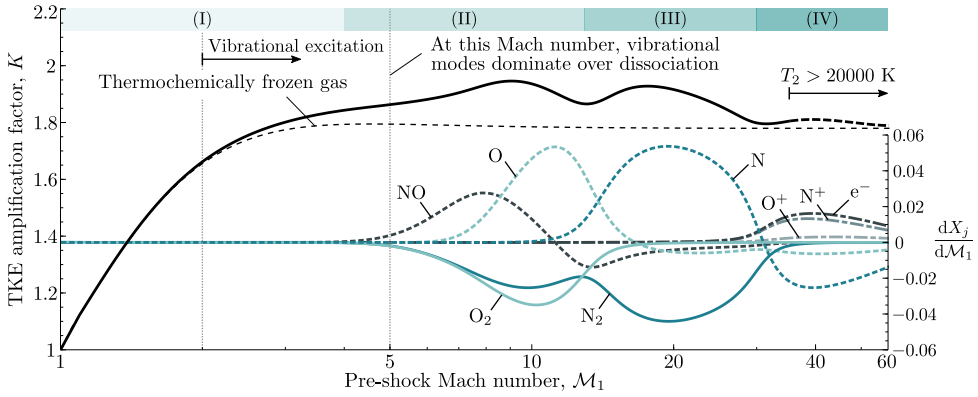

FIG. 5. TKE amplification factor K as a function of the pre-shock Mach number $\mathcal{M}_1$ (upper solid line) for normal shocks propagating in low turbulence intensity air with only vortical deviations ($\chi = 0$) at $T_1 = 300$ K and $P_1 = 1$ atm. The upper dashed line corresponds to the thermochemical frozen gas approximation. The inset represents the rate of change of the molar fractions with the pre-shock Mach number $\mathrm{d}X_j/\mathrm{d}\mathcal{M}_1$ for the most relevant species in the mixture.

dothermicity increases the flow deflection and the generation of transverse kinetic energy; and the RH-slope, which is sensitive to the different internal processes that take place within the non-equilibrium region. The latter is related to the rate of change of the molar fractions with respect to the pre-shock Mach number, $\mathrm{d}X_j/\mathrm{d}\mathcal{M}_1$, for the most relevant species in the mixture, which are also represented in Fig. 5. This is consistent with the observation by Bottin[70] regarding the specific heat capacity at constant pressure c_p, where the author attributed the local maxima in c_p to the dissociation processes of O_2 and N_2, and their subsequent ionization. A simple method to isolate the contribution of the dissociation and ionization of species is to *ad hoc* freeze some of them. For example, when the dissociation and recombination of N_2 is frozen, the first peak of the K-curve still corresponds to the peak of $|\mathrm{d}X_\mathrm{O}/\mathrm{d}\mathcal{M}_1| \sim |\mathrm{d}X_{\mathrm{O}_2}/\mathrm{d}\mathcal{M}_1|$. In this case, higher temperatures are reached due to the absence of the endothermic effects of N_2 dissociation. As a result, the ionization of atomic oxygen occurs at lower Mach numbers, exhibiting the corresponding peak in the TKE curve.

Another effect excluded from our model, but deserving further attention, is the second and subsequent ionization processes of atomic oxygen and nitrogen, which are expected to occur at temperatures exceeding 20,000 K—the upper limit of the NASA polynomials used in this work. To highlight this limitation, a dashed line is shown in Fig. 5 when displaying the computations of the TKE amplification factor above this temperature. By linearly extrapolating the correlation between the sensitivity of dissociation and ionization with the Mach number, we can anticipate that further ionization phenomena, as described in Askari[71], will result in further lower-amplitude peaks in the K vs. $\mathcal{M}_1$ curve.

Figure 6 depicts the amplification of the turbulent intensity, namely

$$\frac{\mathcal{I}_2}{\mathcal{I}_1} = \frac{u_{\ell,2}/\langle u_2\rangle}{u_{\ell,1}/\langle u_1\rangle} = K^{1/2}\mathcal{R}, \tag{32}$$

and the turbulent Reynolds number

$$\frac{\mathrm{Re}_{\ell,2}}{\mathrm{Re}_{\ell,1}} = \frac{u_{\ell,2}\ell_2/\nu_2}{u_{\ell,1}\ell_1/\nu_1} = \frac{K^{1/2}}{\mathcal{T}^{0.7}}\sqrt{\frac{2\mathcal{R}^2+1}{3}} \tag{33}$$

across the shock as functions of the pre-shock Mach number $\mathcal{M}_1$ under the same conditions. In these expressions, u_ℓ represents the velocity fluctuation at the turbulence integral scale ℓ, and ν is the kinematic viscosity of the fluid. Consistent with Huete *et al.*,[47] the turbulent intensity ratio $\mathcal{I}_2/\mathcal{I}_1$ exhibits a sharp increase in regions II and III as species dissociate; see Fig. 6(a). For example, for $\mathcal{M}_1 = 10$, the turbulent intensity is 1.5 times higher than the value predicted for a thermochemically frozen gas, while at $\mathcal{M}_1 \simeq 26$, where maximum amplification occurs, it doubles the predicted value $\mathcal{I}_2/\mathcal{I}_1 \simeq 8$. This maximum corresponds to the turning point of the Hugoniot curve ($\Gamma = 0$, $\mathcal{T} \simeq 42$, and $\mathcal{R} \simeq 12$). For $\mathcal{M}_1 > 26$, the turbulence intensity begins to decrease; however, it is expected to remain higher than the linear extrapolation due to additional species dissociation, ionization, and recombination not accounted for in this study. A similar trend is observed for the turbulent Reynolds number, as illustrated in Fig. 6(b).

b. Vortical with entropic fluctuations As discussed above, the linearized Rankine-Hugoniot equations (28) reveal that, in hypersonic flows, upstream density disturbances may dominate the shock dynamics over velocity and pressure disturbances regardless of whether they are

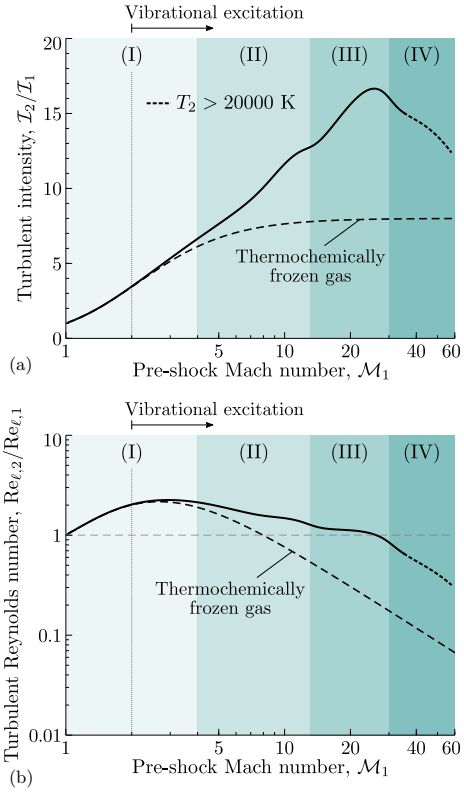

FIG. 6. Amplification of the turbulent intensity $\mathcal{I}_2/\mathcal{I}_1$ (a) and the turbulent Reynolds number $\mathrm{Re}_{\ell,2}/\mathrm{Re}_{\ell,1}$ (b) across the shock as a function of $\mathcal{M}_1$ for air at $T_1 = 300$ K and $P_1 = 1$ atm. The dashed line corresponds to the thermochemical frozen gas approximation. Roman numerals: regions with the dominant reactions labeled in Fig. 3.

entropic[42] or acoustic[41] in nature, a result previously obtained by Mahesh *et al.*[72] and Quadros *et al.*[73] Figure 7 illustrates the variation of the TKE amplification factor K with the pre-shock Mach number $\mathcal{M}_1$ for different degrees of vortical to entropic correlations. In the figure, both thermochemically frozen (dashed lines) and calorically imperfect (solid lines) gas models are included.

The correlation between vortical (ε_r) and entropic (ε_e) fluctuations is quantified by the parameter χ attached to the curves, with positive and negative values indicating different degrees of correlation or anti-correlation, respectively. When the entropic fluctuations are of the same order as the vortical fluctuations, $\varepsilon_e \sim \varepsilon_r$, the degree of correlation is expressed as

$$\langle \chi \rangle = \frac{\langle \delta\rho_1^e \delta u_1^r \rangle}{\langle \delta u_1^r \delta u_1^r \rangle} \frac{\langle c_1 \rangle}{\langle \rho_1 \rangle}. \tag{34}$$

By way of contrast, when the entropic fluctuations scale inversely with the upstream Mach number, $\varepsilon_e \sim \varepsilon_r \mathcal{M}_1^{-1}$, the correlation parameter becomes

$$\langle \chi \rangle = \frac{1}{\mathcal{M}_1} \frac{\langle \delta\rho_1^e \delta u_1^r \rangle}{\langle \delta u_1^r \delta u_1^r \rangle} \frac{\langle c_1 \rangle}{\langle \rho_1 \rangle}, \tag{35}$$

which emphasizes the increasing dominance of vortical structures in shock-turbulence interactions at higher Mach numbers, particularly for $\mathcal{M}_1 > 5$. It is important to note that the sign convention in our definition of χ is opposite to that commonly used in the literature,[72,73] due to the adoption of a different reference frame in our formulation. The bracket symbols denote mean values associated with the upstream turbulence properties, which are considered known inputs for the linear interaction analysis (LIA) shown in Fig. 7.

The results shown in the figure indicate that even relatively small levels of entropic fluctuations, such as $\chi \sim 10^{-2}$, can significantly alter downstream turbulence dynamics. Regarding thermochemical effects, a noticeable change in the curve shape occurs as these effects become active, introducing moderate bumps. However, they play a second-order role in the modulation of the TKE amplification ratio K. For instance, for $\mathcal{M}_1 = 10$ and $\chi = -0.5\mathcal{M}_1^{-1} = -0.05$, K increases by 29% with respect to the purely solenoidal case ($\chi = 0$), while the endothermic effects only contribute an additional 8.6% increase relative to the calorically perfect approximation.

c. Vortical with acoustic fluctuations As mentioned in the discussion following equation (30), density perturbations play a dominant role in the strong-shock limit, regardless of their origin. However, due to the differing correlation properties between steady vortical waves and traveling acoustic perturbations, their quantitative impact varies depending on the nature of the disturbances. We define the dimensionless variable $\eta \sim \varepsilon_a^2/\varepsilon_r^2$, which, in terms of turbulent variables, reads as

$$\eta = \frac{\langle \delta u_{1a}^2 \rangle + \langle \delta v_{1a}^2 \rangle + \langle \delta w_{1a}^2 \rangle}{\langle \delta u_{1r}^2 \rangle + \langle \delta v_{1r}^2 \rangle + \langle \delta w_{1r}^2 \rangle}, \tag{36}$$

which quantifies the relative importance of upstream acoustic versus rotational perturbations. Due to the propagating nature of the acoustic disturbances in the linear regime—unlike the entropic case—the contribution of upstream compressibility to the total kinetic energy can be evaluated independently. The total contribution is then the weighted sum of these components

$$\begin{aligned} K &= \frac{\langle \delta u_2^2 \rangle + \langle \delta v_2^2 \rangle + \langle \delta w_2^2 \rangle}{\langle \delta u_1^2 \rangle + \langle \delta v_1^2 \rangle + \langle \delta w_1^2 \rangle} \\ &= \beta^2 \frac{\langle \hat{u}_2^2 \rangle + \langle \hat{v}_2^2 \rangle + \langle \hat{w}_2^2 \rangle}{\langle \hat{u}_1^2 \rangle + \langle \hat{v}_1^2 \rangle + \langle \hat{w}_1^2 \rangle} = \frac{K^r + \eta K^a}{1+\eta}. \end{aligned} \tag{37}$$

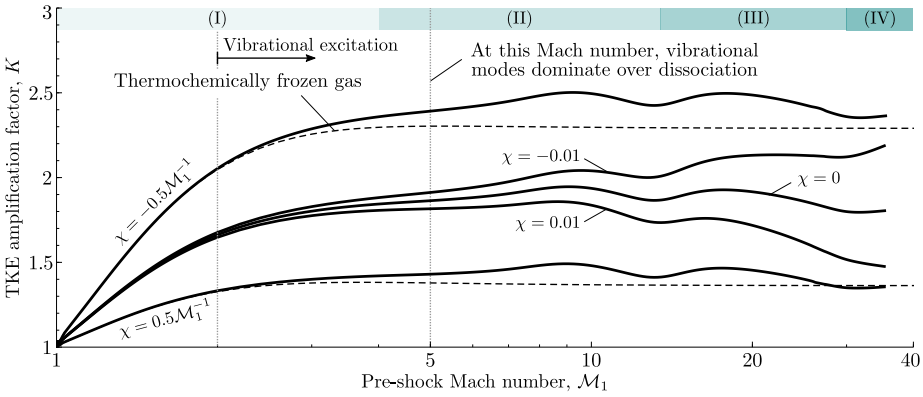

FIG. 7. TKE amplification factor K as a function of the pre-shock Mach number $\mathcal{M}_1$ for normal shocks propagating in low turbulence intensity air with different correlations between vortical and entropic fluctuations χ at $T_1 = 300$ K and $P_1 = 1$ atm. The dashed lines correspond to the thermochemical frozen gas approximation.

By direct inspection in Fig. 8, where the TKE is scaled with the Mach number squared, it becomes clear that, unlike the effect of entropic disturbances analyzed earlier, the contribution of acoustic perturbations can either increase or decrease the downstream kinetic energy. To understand this behavior, we need to focus on the amplification of kinetic energy due solely to upstream acoustic energy, denoted as K^a. This is depicted in Fig. 6(b) of Ref. 74, where the solid line crosses unity at two distinct Mach numbers, $\mathcal{M}_1 = 1.11$ and $\mathcal{M}_1 = 2.35$. Under these conditions, there is no net change in turbulent kinetic energy due to upstream acoustic disturbances, regardless of the amplitude η, as indicated by the intersection of the different curves at these Mach numbers. In the hypersonic regime, the inclusion of compressibility effects in upstream turbulence leads to an increase in turbulent kinetic energy, with an asymptotic contribution that grows with $\mathcal{M}_1^2$. When thermochemical nonequilibrium effects are considered, a similar trend is observed, though with slightly different Mach numbers at the intersection points. In addition, hypersonic effects render the expected double-peak contribution associated with high endothermicity.

From the study of the previous cases involving vortical and vortical-entropic fluctuations (see Figs. 5 and 7), it is evident that thermochemical effects have only a secondary effect on the amplification of K. However, when the incoming turbulence is compressible, i.e., $\eta > 0$, the observed amplification is significantly larger compared to the purely vortical case, where $\eta = 0$. In this scenario, compressibility effects dominate the leading order behavior, underscoring why compressible fluctuations cannot be neglected *a priori* in the hypersonic regime, even when compressibility is less than 10%. In such conditions, the interplay between compressibility and thermochemical effects becomes increasingly relevant, with both mechanisms contributing substantially to the overall amplification dynamics.

C. Flight altitude effects

The flight envelope of hypersonic air-breathing vehicles presents lower and upper altitude limits beyond which the vehicle cannot be flown. The lowest altitude limit is constrained by structural aircraft capabilities, while the highest altitude is imposed by the engine combustion requisites that demand a minimum amount of oxygen to operate. Briefly speaking, a cruise hypersonic aircraft must fly between 15–30 km at Mach-5 and 30–45 km at Mach-15.[75] Then, since atmospheric properties are susceptible to altitude changes of the order of 10 km, it is natural to wonder how this effect modifies the TKE amplification factor computed above.

Before computing the function K vs. $\mathcal{M}_1$, it is convenient to recall an assumption underlying the LIA: the thickness ℓ_T of the thermochemical nonequilibrium region behind the shock must be much smaller than the characteristic size of the shock wrinkles, which is of the same order as the integral length scale of the free-stream turbulence ℓ. Thus, to properly assess the assumption $\ell \gg \ell_T$, we must evaluate the characteristic length of the chemical nonequilibrium region as a function of the flight altitude for a representative flight Mach number, say $\mathcal{M}_1 = 10$. To this end, we use the Hypersonic Task-based Research (HTR) solver.[8,9,76] The HTR solver is a high-order Navier–Stokes solver targeted towards direct numerical simulations of chemically-reactive compressible turbulent flows. In particular, we utilize a recent update of the HTR solver[77] that describes thermochemical nonequilibrium via a two-temperature model.[59] This

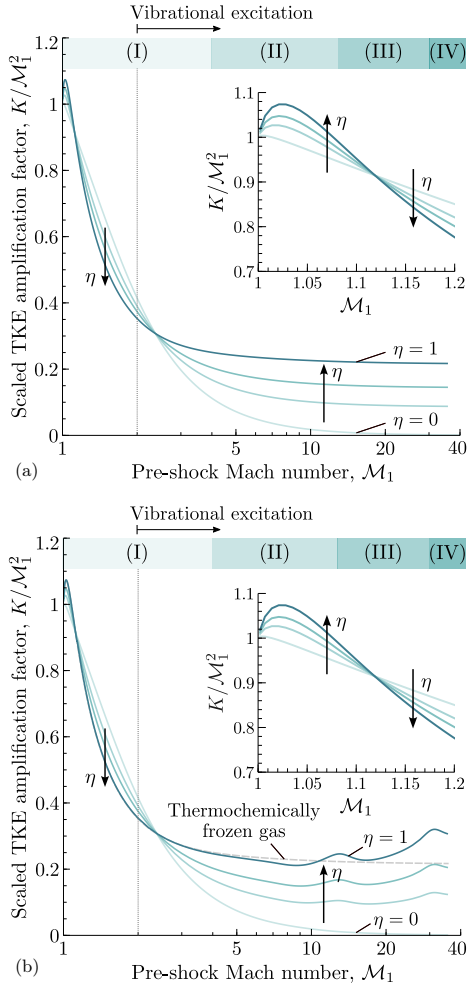

FIG. 8. Scaled TKE amplification factor $K\mathcal{M}_1^{-2}$ as a function of the pre-shock Mach number $\mathcal{M}_1$ for normal shocks propagating in air with different vortical and acoustic deviations $\eta = [0, 0.25, 0.5, 1]$, at $T_1 = 300$ K and $P_1 = 1$ atm. Panel (a) represents the calorically perfect gas solution, while panel (b) displays results considering a calorically imperfect gas.

type of model uses two temperatures: T, related to the translational and rotational energy modes of the chemical species in the gas, and T_{ve}, related to vibrational and electronic excitation. The dissociation rate constants are evaluated at the geometric mean temperature $\sqrt{TT_{ve}}$. The chemistry of air (79% N_2, 21% O_2 in volume) is modeled with a 5-species mixture {N_2, O_2 NO, O, N} using NASA's 9-coefficient polynomials. The interested reader is referred to Di Renzo *et al.*,[8] Di Renzo and Pirozzoli,[9] and Di Renzo[76] for further details on the numerical solver itself. The calculations are carried out in a one-dimensional computational domain discretized with 1200 grid points. Supersonic inflow conditions are imposed at the upstream boundary, while the downstream boundary features a characteristic multi-component non-reflecting outflow boundary condition.[62,78] Calculations are advanced in time with a constant time step that implies a Courant–Friedrichs–Lewy number CFL ~ 0.1, until a steady state is reached.

The numerical results are displayed in the insets of Fig. 9, where the upstream pressure (left subplot) is plotted versus the thermochemical relaxation length for $\mathcal{M}_1 = 10$ at different flight altitudes in the International Standard Atmosphere (ISA).[79] The right subplot represents the temperature profile of the nonequilibrium zone at an altitude of 10 km above mean sea level. The characteristic relaxation length ℓ_T, shown as a diamond symbol, is found to grow from $\sim 10^{-4}$ m to $\sim 10^{-2}$ m as the flight altitude increases from 0 to 30 km. As a result, the minimum characteristic length of the turbulent eddies that can be described using the LIA increases correspondingly with the flight altitude. During the climb and acceleration segment, the value of ℓ_T is expected to decrease as the Mach number increases (since the post-shock temperature increases with the Mach number) and to increase as the altitude increases (because of the exponential pressure drop with altitude), the latter being the expected dominant contribution. This is better analyzed by looking at Fig. 9(b), which shows the temperature and pressure profiles in the ISA model. First, the temperature decreases linearly in the troposphere (from sea level to 11 km), it remains roughly constant at the lower layer of the stratosphere (from 11 km to 20 km), and finally increases again until reaching the mesosphere at 50 km of altitude. By contrast, the pressure exhibits a monotonous power-law decay with altitude that becomes exponential in the constant temperature layer from 11 km to 20 km.

Returning to the TKE amplification factor, we refer again to Fig. 9, which shows the variation of K with the pre-shock Mach number $\mathcal{M}_1$ at five flight altitudes: 0, 5, 10, 20, and 30 km above sea level. For all cases, the qualitative picture remains the same, with small changes associated with the variation of the upstream conditions with altitude. In general, endothermic effects are found to increase the value of K across the whole Mach number range. Moreover, the higher the altitude, the stronger the peaks in the amplification of the turbulent kinetic energy. It must be emphasized that K represents the TKE amplification factor, meaning that the evaluation of the total turbulent intensity requires information on the upstream turbulent flow, which is also expected to change with flight altitude. In this case, lower (higher) pre-shock temperatures shift the curves

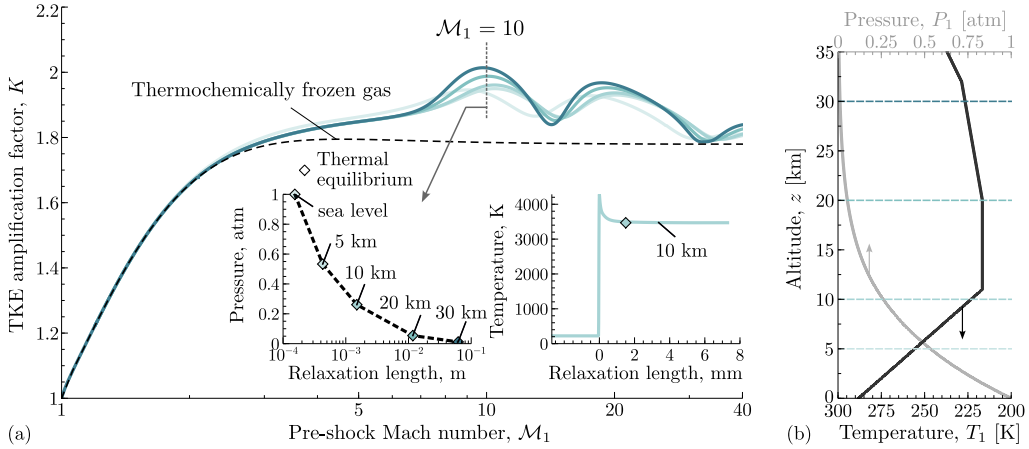

FIG. 9. TKE amplification factor K as a function of the pre-shock Mach number $\mathcal{M}_1$ at different flight altitudes (0, 5, 10, 20, and 30 km) above sea level in the ISA model (a) and the corresponding temperature-pressure vs. altitude profiles (b). The curve for the lowest altitude (0 km) corresponds to conditions indicated in Fig. 5. The dashed line corresponds to the thermochemically frozen gas approximation. The insets represent the variation of the pressure (left) and temperature (right; translational and rotational) with the relaxation length as obtained from one-dimensional direct numerical simulations with the HTR solver[8,9,76] using a two-temperature model. A. Cuadra, M. Vera, M. Di Renzo and C. Huete, AIAA SciTech 2023 Forum, 2023–0075, 2023;[55] licensed under a Creative Commons Attribution (CC BY) license.

to the right (left), which means that a higher (lower) pre-shock velocity is required to achieve similar conditions. Flight altitude also affects the integral length scale of the upstream turbulence, making the conditions imposed by LIA ($\ell_T \ll \ell$) less likely to occur. The effect of turbulent perturbations with a characteristic length of the order of the thermochemical relaxation length is out of the scope of this work, but it can be investigated using direct numerical simulations, as done by Kerkar and Ghosh.[60] Their findings suggest chemical reactions within the nonequilibrium region enhance the production of turbulence, primarily due to the amplification of streamwise velocity perturbations, as opposed to the laterally dominating turbulence predicted by LIA.

III. NUMERICAL SIMULATIONS

Turbulence and shock waves interact in various flow problems relevant to supersonic and hypersonic flight. This entails, for instance, deflected control surfaces or shock-based lifting bodies (waveriders) in external flows, or intakes and isolators of air-breathing propulsion flow paths. The canonical STI setup, shown in Fig. 1, represents the simplest model of how turbulence and shock waves interact with each other. In its simplest form, isotropic turbulence is convected through a normal shock wave, where a few parameters define the type of interaction (see Sec. I). The isolated setup enables furthering the fundamental understanding of the interaction's mechanism and drives the numerical framework required to study the problem accurately. The numerical approach requires low dissipation for the turbulence part, while an increased dissipation is needed to capture the shock wave, particularly at higher pre-shock Mach numbers.

This section presents a comprehensive review of the numerical work devoted to the canonical STI problem. The overview adopts a grouping based on numerical frameworks and STI subtopics of interest (Sec. III A), and continues by compiling key results from the literature (Sec. III B) alongside direct comparisons with relevant advancements in LIA, discussed earlier in Sec. II A. These comparisons highlight the specific developments related to hypersonic flows, which illustrate deviations from the assumptions of a calorically perfect gas.

A. Literature Review

The following review summarizes key developments in the numerical simulation of shock-turbulence interaction, focusing on both direct numerical and large-eddy simulation approaches. To start, numerical frameworks for solving the compressible Navier-Stokes equations are considered, followed by a review of direct numerical simulation for the canonical shock turbulence interaction. Finally, key conclusions pertaining to subgrid-scale modeling and large-eddy simulation are presented from the

shock-turbulence literature.

1. Numerical frameworks

The main challenge in performing a numerical investigation of STI comes from the conflicting requirements of stability and accuracy.[80] To capture the correct dynamics of turbulence one needs to select a numerical scheme that adds as little dissipation as possible to preserve the Reynolds number of the flow. On the other hand, the presence of discontinuities can easily induce instability of the calculations via Gibbs artifact if not treated correctly. Several solutions have been devised to address these competing effects, which may be classified into three categories.

The first category seeks to discretize the shock wave assuming its thickness is similar to the laminar value and calculations performed with this strategy are referred to as "shock-resolving". Moin and Mahesh [81] demonstrated that the ratio between the Kolmogorov length scale of the incoming turbulence (η_k) and the shock wave thickness (δ) scales as

$$\frac{\eta_k}{\delta} = 0.13\sqrt{Re_\lambda}\frac{\mathcal{M}_1 - 1}{\mathcal{M}_t}. \tag{38}$$

If this ratio is order unity, one could aim at using a single discretization scheme for the Navier-Stokes equations inside and outside the shock wave. It is clear however that this strategy becomes rapidly unfeasible as soon as the upstream Mach number exceeds 1.5. This class of numerical framework, which has been utilized in studies of weak interactions,[21–23] is therefore unsuitable for evaluation of strong shocks and will not be further discussed in this review about hypersonic shock-turbulence interactions.

The second type of framework is referred to as "shock-capturing" and it regularizes the presence of discontinuities by adding numerical dissipation to stabilize the solution. As this numerical dissipation can strongly influence the accuracy of turbulence prediction, it is critical to carefully select the regions where stabilization is required. For this reason, several algorithms have been developed and utilized over the years to predict canonical STI. Numerical dissipation is either added by locally changing the numerical scheme to a dissipative formulation or artificially introducing additional viscosity in the flow. The former approach has been mainly applied by considering non-linear shock-capturing schemes, such as Essentially-Non-Oscillatory (ENO),[82] Weighted-ENO (WENO),[83] Targetted-ENO (TENO),[84] and their variants, combined with flux-splitting methods. As these non-linear schemes might still prove significantly dissipative, a common approach is to mix them with centered schemes creating what is termed a hybrid discretization. Specifically, a selection process based on a sensor is utilized to distinguish smooth regions of the flow from stencils that go across shocks. In this way, energy-preserving formulations can be deployed in smooth regions of the flow, while shock-capturing is limited to the vicinity of shock waves. Examples of works that utilized this technique for STI studies are due to Lee *et al.*,[85] and Larsson and Lele.[46] It is noteworthy that the overall numerical dissipation strongly depends on the specificity of the considered shock sensor, and, for this reason, recent works are focusing on deriving more advanced and precise sensors.[61,86] The idea of including additional dissipation by means of an artificial viscosity was first proposed by von Neumann and Richtmyer,[87] and Jameson *et al.*[88] and then developed in several different forms by others, particularly in the context of Large-Eddy Simulations (LES).[89,90] This approach, which is less invasive in the overall numerical algorithm of a code, provides similar stabilization properties as the ENO-type approach, though some extra dissipation is sometimes observed. In both shock-capturing approaches, a computational grid size large enough to capture all the scales of the shock wave wrinkling is necessary. A thorough review of the shock-capturing framework performance in the context of STI direct numerical simulation is provided by Johnsen *et al.*[6]

The third class of numerical frameworks is the "shock-fitting", whereby the shock-wave is treated as a pure discontinuity, and Rankine-Hugoniot jump conditions are considered across the nodes of the computational grid[91]. This methodology is inherently more costly from a computational point of view, though its ability to consider strong shock waves without introducing additional dissipation, might be particularly beneficial in computing hypersonic STI. For this reason, experiments of very intense STI calculations have been performed over the years[92–95] though the Reynolds number of the interactions has always remained low to avoid excessive computational cost.

Most studies involving canonical STI have been performed using one of the aforementioned shock treatments in conjunction with a finite-difference (FD) discretization of the Navier-Stokes equations. In fact, the simple geometrical configuration of these interactions has favored the use of FD schemes, which are usually easy to implement using high-order discretization necessary to achieve an accurate representation of turbulence at moderate computational cost. Typical FD schemes utilized in STI for the smooth region of the flow are either skew-symmetric[96,97] or compact.[98] However, the need to extend the study of STI to more complicated configurations has motivated the development of finite volume[35,99–101] and discontinuous Galerkin[102–104] formulations with satisfactory results.

2. Direct numerical simulation

The direct numerical simulations of Lee[21,22,85] comprised the first fully nonlinear analysis of shock-turbulence interaction, enabling a detailed characteriza-

tion of the evolution of turbulence statistics throughout the interaction. These simulations confirmed that the interaction of vortical isotropic turbulence with a shock wave leads to an amplification of turbulence kinetic energy, together with a corresponding reduction in the characteristic turbulence length scales due to preferential amplification of small-scale (i.e., high-wavenumber) turbulence motion.[22] Substantial agreement between the fully nonlinear numerical simulations with LIA implies this augmentation of turbulence kinetic energy arises primarily from linear mechanisms. In addition to reproducing TKE amplification, linear interaction analysis was likewise shown to correctly predict a reduction in the Taylor length scale across the interaction, as well as the Mach-number dependence for the post-shock variation in the Kolmogorov scale.[85] In particular, LIA and DNS both corroborated that at modest bulk Mach numbers, i.e., $\mathcal{M}_1 < 1.65$, the post-shock dissipation scale is increased relative to the pre-shock turbulence, while further increasing the Mach number gives rise to a reduction in the Kolmogorov scale across the interaction. As such, the resolution requirements of direct numerical simulation were confirmed to be heightened through the interaction for high supersonic and hypersonic Mach numbers, necessitating post-shock refinement to maintain a constant grid spacing relative to the local Kolmogorov scale.[46,85] This aspect has so far limited the execution of direct numerical simulations in the hypersonic regimes at high Reynolds numbers. The highest investigated pre-shock Mach numbers remain in the neighborhood of $\mathcal{M}_1 \sim 5$ and have been considered only in conjunction with moderate Reynolds numbers based on the Taylor microscale ($\mathrm{Re}_\lambda \sim 40$).[46,56,105,106] In contrast to LIA's success in predicting turbulence kinetic energy and length-scale evolution across canonical shock turbulence interaction, the linear theory was proven to be unable to capture the evolution of post-shock anisotropy, which arises primarily from further augmentation of the streamwise normal component of the Reynolds stress tensor via pressure-transport effects following the primary interaction.[22]

Relative to the purely vortical isotropic turbulence considered by Lee,[21,22,85] the introduction of entropic modes, associated with correlated velocity/temperature fluctuations upstream of the shock, was subsequently shown utilizing direct numerical simulation to further augment TKE amplification across the interaction for negative correlations.[35,72] The presence of positively correlated velocity/temperature fluctuations correspondingly diminished the TKE amplification. For both positively and negatively correlated temperature/velocity fluctuations, Mahesh[72] demonstrated that the modulation of post-shock TKE amplification by entropic modes arises from the baroclinic torque induced by upstream density fluctuations. Furthermore, the presence of upstream dilatational energy, associated with intrinsic compressibility in the pre-shock turbulence, likewise serves to further augment the TKE amplification, particularly at elevated bulk Mach numbers, as evidenced by the numerical simulations of Grube and Martin[105] and Cuadra *et al.*[56]

The study of non-linear interactions between turbulence and shock waves has also led to the identification of three primary regimes of the shock deformations.[46,64,107–111] When the upstream perturbations are weak, the shock wave remains coherent, and its position is only locally displaced upstream and downstream with respect to its mean location. If the turbulence perturbations that impinge upon the shock are sufficiently strong, they prove able to locally alter the intensity of the discontinuity and even generate holes within its front. These two regimes were identified at first by Larsson[46] and are termed "wrinkled" and "broken", respectively. Much later, Chen and Donzis[110] demonstrated that a third regime arises when pre-shock turbulence fluctuations become very intense. This new state, the so-called "vanished" regime, corresponds to conditions where the shock is not able to produce any amplification of the Reynolds stresses, while the mean-field jump conditions remain satisfied. The transition from the wrinkled to the broken shock regime appears to be well described by the parameter $\mathcal{K} = \mathcal{M}_t/(\mathcal{M}_1 - 1)$. For $\mathcal{K} > 0.6$ the shock will be broken, whereas otherwise, it will be subject to wrinkling.[46,64] The appearance of the vanished state seems instead correlated with the scale-separation parameter $\delta/\eta_k \sim 7.69$. It is noteworthy that as the pre-shock Mach number increases, both δ/η_k and $\mathcal{K}$ decrease, making the appearance of broken or vanished shocks unlikely in hypersonic flows. However, the confinement of the shock response to the wrinkled regime favors the agreement between LIA and DNS results for highly hypersonic conditions. In fact, several studies have shown that, in supersonic conditions, having a low δ/η_k emerges as a determining factor for achieving convergence between LIA and DNS.[63,110,112–114]

3. Large-eddy simulation

Reducing the overall degrees of freedom, and therefore computational cost, relative to direct numerical simulation, large-eddy simulation (LES) instead provides a coarse-grained representation of shock-turbulence interaction. As LES entails directly resolving only the largest turbulence length scales, modeling the effect of physical processes transpiring beneath the grid scale, i.e. subgrid scale (SGS), is required. Formally, this closure problem in the low-pass-filtered momentum equation comprises the right-hand side of

$$\begin{aligned}\frac{\partial}{\partial t}(\overline{\rho}\widetilde{u_i}) + \frac{\partial}{\partial x_j}\left(\overline{\rho}\widetilde{u_i}\widetilde{u_j} + \overline{P}\delta_{ij} - \hat{\sigma}_{ij}\right) \\ = \frac{\partial}{\partial x_j}\left(\tau_{ij}^{\mathrm{SGS}} + \mathcal{V}_{ij}^{\mathrm{SGS}}\right)\end{aligned} \tag{39}$$

where $\overline{\rho}$ is the filtered density, $\widetilde{u_i} = \overline{\rho u_i}/\overline{\rho}$ is the Favre-filtered velocity, and $\hat{\sigma}_{ij}$ is the viscous stress tensor as

evaluated with the resolved primitive variables. The unclosed terms arising from the nonlinearity in the Navier-Stokes equations, i.e., those which cannot be trivially expressed in terms of the filtered variables, consist of the subgrid stress tensor $\tau_{ij}^{\mathrm{SGS}} = \overline{\rho}(\widetilde{u_i u_j} - \widetilde{u_i}\widetilde{u_j})$ and the subgrid viscous stress $\mathcal{V}_{ij}^{\mathrm{SGS}} = \hat{\sigma}_{ij} - \overline{\sigma}_{ij}$, with $\overline{\sigma}_{ij}$ denoting the filtered viscous stress tensor. Within the LES formalism, while the closure of the continuity equation proves trivial when expressed in terms of the filtered density and Favre-averaged velocity, the evolution of the temperature field typically entails numerical solution of a filtered energy equation[115,116] or total-energy equation as constructed based on the filtered primitive variables themselves.[23,117,118]

Whereas closure of the subgrid viscous stress, as well as the analogous closure terms involving molecular diffusivities, is generally neglected on the basis of *a priori* analysis[117] and scale-separation arguments, LES predictions of shock-turbulence interaction have been shown to depend sensitively on the closure of the (inviscid) subgrid stress tensor, typically modeled on the basis of the eddy-viscosity approximation, namely $\tau_{ij}^{\mathrm{SGS}} = 2\mu_t \widetilde{S}_{ij}$ where μ_t is the effective eddy "viscosity" and $\widetilde{S}_{ij}$ is the Favre-averaged strain-rate tensor.[99] In particular, the early study of Garnier *et al.*[119] demonstrated that inclusion of the explicitly-modeled subgrid stress from the Dynamic Smagorinsky model[120,121] provided significant improvement in the prediction of the filtered turbulent kinetic energy and Reynolds stresses for well-resolved calculations, relative to both coarsened DNS and the static Smagorinsky model, which proved under- and over-dissipative, respectively. At coarser resolutions, namely when the shock corrugations become subgrid, Garnier *et al.*[119] likewise demonstrated that LES-based predictions of the canonical shock-turbulence interaction deteriorate significantly, not necessarily due to breakdown of the post-shock subgrid model performance but instead due to insufficient resolution of the shock wave itself. Subsequent coarse-grid LES calculations by Bermejo-Moreno *et al.*,[122] for which the nominal spanwise grid spacing exceeded that of the DNS by a factor of 16, similarly suggest that even the state-of-the-art LES approaches naturally yield inaccurate predictions of the Reynolds-stress evolution through the canonical shock-turbulence interaction at such coarse resolutions.

In conjunction with the finding that high-fidelity LES of canonical shock-turbulence interaction requires direct resolution of shock corrugations by the grid, LES predictions have likewise been shown to improve significantly by setting the subgrid fluxes to zero in cells for which a shock-capturing scheme is active, limiting the activation of the explicit SGS models to cells for which a central numerical scheme is utilized to evaluate the resolved inviscid fluxes.[122] In this way, deactivation of the SGS models in the vicinity of the shock precludes SGS dissipation from further augmenting the numerical dissipation introduced by the shock-capturing scheme. Recently, by leveraging adaptive mesh refinement to ensure resolution of shock corrugations and limited activation of subgrid fluxes away from detected discontinuities, Braun *et al.*[123] recently developed an explicit large-eddy simulation framework based on a hybrid stretched-vortex model,[124] producing resolved Reynolds-stress profiles largely independent of the post-shock resolution for high-Re_λ upstream turbulence.

To date, this joint development and assessment of large-eddy simulation models for shock-turbulence interaction have focused almost entirely on supersonic flows. However, as the free stream Mach number increases, several key physical processes emerge, which will demand novel subgrid-scale modeling. In particular, as the turbulent Mach number through the interaction increases, giving rise to increasingly significant dilatational motion, treatment of the isotropic component of the subgrid stress tensor becomes increasingly important.[121,125,126] Representing the subgrid kinetic energy, τ_{kk}^{SGS} must be modeled to close not only the filtered momentum equations but the energy-transport equation as well.[127] As the bulk Mach number further increases and viscous dissipation gives rise to high-temperature post-shock conditions, finite-rate thermochemical effects emerge, including vibrational excitation, chemical dissociation, and ionization. Filtering of the relevant vibration-energy conservation and species' continuity equations gives rise not only to additional subgrid advective closure problems for the transport of vibrational energy and partial densities but subgrid contributions to the reactive and thermal relaxation processes as well. Analysis of explicit subgrid modeling approaches for thermochemical relaxation in the context of hypersonic large-eddy simulation has been the subject of only limited investigation in the literature,[128,129] and therefore represents a key area for future development to enable coarse-grained calculations of shock-turbulence interaction at high Mach numbers.

B. Compilation of numerical results

Following the CFD overview in Sec. III A, some of the DNS results on STI are presented herein. Table I summarizes the upstream conditions adopted by various authors in canonical STI studies for calorically perfect gases,[22,37,46,72,85,105,110–112,130–132] and more recently, for thermally perfect gases with compressibility effects at Mach 5.[56] Over the past two decades, significant progress has been made in understanding the complex physics governing STI. As shown in Fig. 10, a substantial amount of DNS data has been gathered over a wide range of upstream Mach numbers, $\mathcal{M}_1 \in [1.1, 6]$, turbulent Mach numbers $\mathcal{M}_t \in [0.02, 0.691]$, and Taylor Reynolds numbers, $\mathrm{Re}_\lambda \in [9, 74]$. The upstream conditions are presented in a linear-log fashion as a function of the factor $\mathcal{M}_1 - 1$ for better visualization. The data covers different types of shock regime as defined based on the similarity parameter provided by Larsson *et al.*[37] Despite these advances, the hypersonic regime, defined by $\mathcal{M}_1 \geq 5$

(highlighted in grey), remains largely unexplored due to the significant computational demands imposed by strong shocks, which exacerbate the inherent complexities of thermochemical non-equilibrium flows. Furthermore, achieving the ultimate goal of simulating fully developed turbulence in the STI problem, which requires $\mathrm{Re}_\lambda > 100$,[113,133] remains a formidable challenge, as will be discussed in Sec. IV.

Since Fig. 10 only depicts the input parametric space explored in STI through DNS, they do not provide information on the turbulence amplification ratio. This ratio is presented and compared with far-field predictions using the LIA framework in Figs. 11 and 12. The LIA results, based on the analysis presented int Sec. II B, consider both calorically perfect and calorically imperfect gases. It must be noted that accurately determining the precise value from the DNS data for direct comparison with the LIA results can be challenging because the shock-capturing method typically involves numerical dissipation factors that have an impact on the turbulence evolution. To define the far-field solution in the DNS, several works (see e.g., Chen and Donzis [110,111]) take advantage of the non-monotonic behavior of the streamwise Reynolds stress (R_{11}). In particular, the position at which the streamwise Reynolds stress peaks, typically normalized with its corresponding upstream value ($R_{11}/R_{11,1}$), is the position at which the comparison is carried out. Alternatively, one can extrapolate the turbulent statistics back to the average shock position, as suggested by Larsson and Lele.[46] This approach aims to minimize the influence of viscosity effectively. Additional discrepancies may also arise because LIA results are derived from Reynolds-averaged statistics, while DNS of compressible flows commonly relies on Favre-averaged statistics. The latter choice is proved convenient when dealing with the convective term of the Navier-Stokes equations.

We first focus on the longitudinal and transverse components of the turbulent kinetic energy, quantified by the streamwise Reynolds stress R_{11} and the transverse Reynolds stress R_{22}. Both LIA (lines) and DNS data (markers) are presented in Fig. 11. In particular, solid lines correspond to a calorically imperfect gas in thermochemical equilibrium, while dashed lines assume the calorically perfect approximation with a constant adiabatic index $\gamma = 1.4$. The LIA predictions are color-coded from light-to-dark blue, reflecting increasing upstream compressibility levels, denoted by $\eta = [0.001, 0.05, 0.1]$. The remaining input parameters for the simulations at $\mathcal{M}_1 = 5$, provided in Table I and corresponding to Cuadra *et al.*,[56] were selected with the aim of enabling a direct comparison with LIA. Similar DNS setups, which disregard non-linearities and viscous effects not captured by LIA, are represented using the same color scheme for consistency and presented in a log-log scale as a function of the factor $(\mathcal{M}_1 - 1)$ for better visualization. In particular, light-to-dark blue circles and squares denote their results for $\gamma = 1.4$ and $\gamma = \gamma(T)$, respectively. The

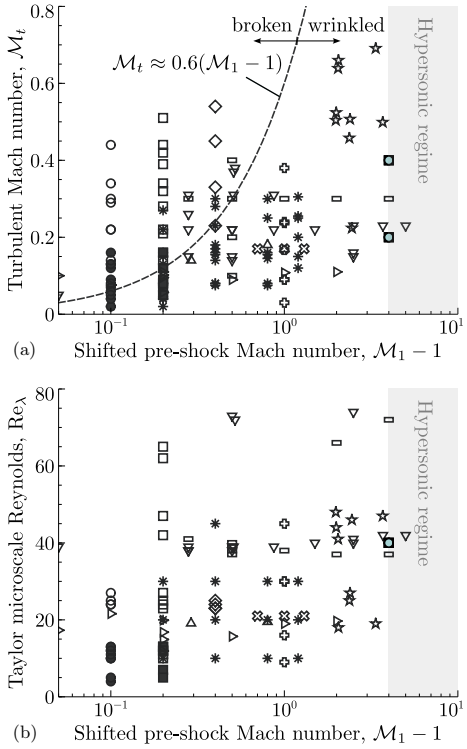

FIG. 10. Compilation of upstream conditions considered in direct numerical simulations for solving the shock-turbulence interaction problem, displaying (a) turbulent Mach number and (b) Taylor Reynolds number as functions of the Mach number. The dashed line denotes the limit from broken to wrinkle regime proposed by Donzis.[63,64] The grey area denotes the hypersonic regime $\mathcal{M}_1 \geq 5$. The symbols represent direct numerical simulations from other studies: (▷),[22,85] (△),[72] (▽),[37,46] (∗),[112] (✜), [130] (⊠),[131] (○,●,□,■,◇),[110,111] (▭),[132] (☆),[105] and (●,■).[56]

data collected from other numerical simulations, not corresponding to the hypersonic regime, are denoted by different symbols (see Table I for reference), maintaining the notation of Chen and Donzis[110,111] for the results presented there. For example, the hollow symbols represent results obtained using HIT, while the black filled symbols correspond with spatially developed turbulence (SDT), which allows the interaction between the fluctuations and the mean flow. This procedure resembles a larger streamwise component of velocity variance compared to the transverse components (slightly anisotropic flow), similar to the conditions found in wind tunnel tests.[110,134]

TABLE I. Summary of several computational works in canonical shock-turbulence interactions.

Source	Year	$\mathcal{M}_1$	$\mathcal{M}_t$	Re_λ	γ	Symbol
Lee *et al.*[22,85]	1993, 1997	1.2, 2, 3	0.102-0.11	14.9-19.7	1.4	▷
Mahesh *et al.*[72]	1997	1.29	0.14	19.1	1.4	△
Larsson *et al.*[37,46]	2009, 2013	1.28-6	0.05-0.56	39-74	1.4	▽
Ryu and Livescu[112]	2014	1.1-2.2	0.02-0.27	10-45	1.4	∗
Tian *et al.*[130]	2017	2	0.09-0.38	9-45	1.4	✜
Boukharfane *et al.*[131]	2018	1.7, 2, 2.3	0.17	21	1.4	⊠
Chen and Donzis[110,111]	2019, 2022	1.1, 1.2, 1.4	0.05-0.54	10-65	1.4	○,●,□,■,◇
Gao *et al.*[106]	2020	1.28-5	0.1-0.4	37-74	1.4	▭
Grube and Pino[105]	2023	2.98-4.69	0.224-0.691	18-48	1.4	☆
Cuadra *et al.*[56]	2024	5	0.2, 0.4	40	1.4, $\gamma(T)$	○, □

By direct inspection of Fig. 11, it is observed that the two components of the Reynolds stresses are amplified in most of the region tested. For the purely solenoidal case ($\eta = 0$), at pre-shock Mach numbers up to $\mathcal{M}_1 \sim 2$, most of the TKE produced across the shock belongs to rotational modes of the streamwise velocity fluctuations (the acoustic contribution is negligible in the far-field for $\eta = 0$). However, for $\mathcal{M}_1 \gtrsim 2$, R_{11} plunges below R_{22} and the transverse component dominates, reaching its first peak around $\mathcal{M}_1 \sim 10$. This value is approximately 15% higher than the obtained with the thermochemically frozen approximation. In contrast, when dilatational modes are present ($\eta > 0$), as in the case of $\eta = 0.1$, the acoustic contribution of the TKE amplification accounts for approximately $\sim 3\%$ for a Mach-2 and 5% at Mach-5. More significantly, even with a modest upstream compressibility of 5%, both R_{11} and R_{22} show notable amplification as $\mathcal{M}_1$ increases. For instance, at $\mathcal{M}_1 = 5$, LIA predicts an amplification of around 42% for R_{11} and 16% for R_{22} with $\eta = 0.05$, while with $\eta = 0.1$, these values rise to approximately 80% and 31%, respectively, compared to the purely solenoidal case with $\gamma = 1.4$. The Reynolds stresses components are further modulated when accounting for high-temperature endothermic effects. For example, with $\eta = 0.1$, LIA predicts a 7% decrease in R_{11} and an increase of 5% in R_{22}. Note that at Mach-5 vibrational excitation dominates over the dissociation process. However, it is readily seen how the caloric imperfect solution deviate more from the $\gamma = 1.4$ case as $\mathcal{M}_1$ exceeds 5.

Therefore, we can conclude that, although discrepancies between the final values of R_{11} and R_{22} in LIA and DNS are observed, as expected under the conditions explored by Cuadra *et al.*,[56] the relative impact of compressibility effects at Mach 5 are accurately captured. In particular, the light-to-dark blue symbols indicate varying degrees of compressibility, with circles and squares representing the caloric perfect and caloric imperfect approximations, respectively. In all the cases tested, the Reynolds stresses R_{11} (panel a) and R_{22} (panel b) increase as compressibility levels rise, as predicted by LIA. On the other hand, with regard to high-temperature endothermic effects, LIA predicts a decrease in R_{11} and an increase in R_{22}, whereas DNS results show amplification in both components. This translates into an different prediction is what concerns the turbulence anisotropy: the one predicted by LIA ($R_{22} > R_{11}$) is totally opposite to the DNS ($R_{11} > R_{22}$). Although this effect tends to balance out when considering the total kinetic energy, as discussed later, further studies are needed to fully understand the discrepancies. One plausible explanation[47] is that LIA overpredicts the transverse velocities due to its idealization of transverse velocity conservation across the shock, particularly in non-equilibrium regions. The endothermicity and the higher compression ratio result in a greater local deflection than that computed with a finite non-equilibrium zone. Consequently, the overprediction of lateral velocity leads to an underprediction of the streamwise component, based on the conservation of energy. Further explanations pertain to the energy transfer occurring from the acoustic field in the longitudinal direction. This phenomenon leads to DNS predictions for R_{11} being higher than those provided by LIA when $\mathcal{M}_1 \gtrsim 2.5$.

With use made of the Reynolds stresses, R_{11} and R_{22}, it is straight forward to construct the total TKE amplification factor according to $K = 1/3(R_{11} + 2R_{22})$, as shown in Fig. 12. Here, the DNS data from Larsson and Lele[46] and Larsson *et al.*[37] are also included (red symbols). These DNS results correspond to a slightly different setup, in which the authors artificially eliminated viscous dissipation by extrapolating to an infinite Reynolds number [see Eq. (3.4) from Ref. 37]. It was found that, in contrast to the values obtained for the independent Reynolds stresses R_{11} and R_{22}, the total TKE amplification factor produced by DNS is much closer to the LIA prediction. As expected, the DNS results approximate LIA prediction when $\mathcal{M}_t \ll 1$ and $\mathrm{Re}_\lambda \to \infty$. Specifically, similar values are obtained when there is sufficient separation of scales between the characteristic size of the smallest eddies and the shock thickness. Previous studies also confirm the convergence between LIA and DNS when the turbulent Mach number approaches zero.[110,112] Regarding the effects of upstream compress-

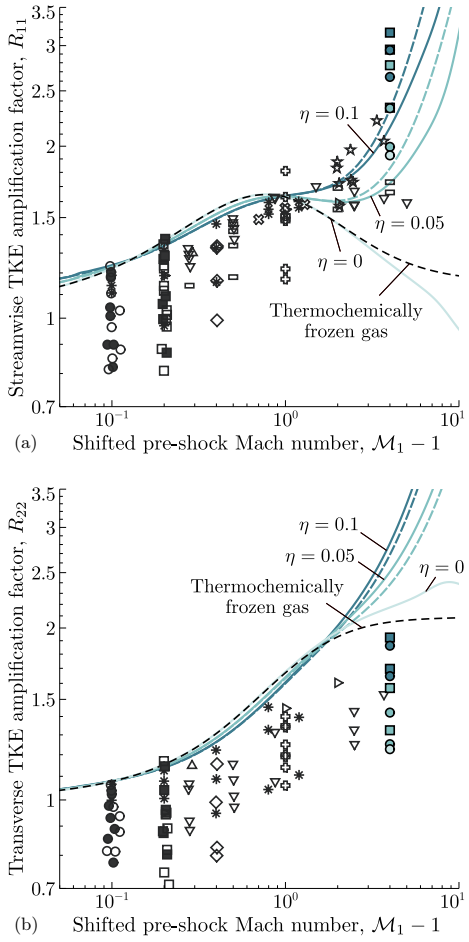

FIG. 11. Streamwise R_{11} (a) and transverse R_{22} (b) components of the TKE amplification factor as a function of $\mathcal{M}_1 - 1$. The dashed lines correspond to the values of R_{11} and R_{22} calculated assuming that the post-shock gas is thermochemically frozen. The symbols represent direct numerical simulations from other studies: (▷),[22,85] (△), [72] (▽),[37,46] (∗),[112] (✣),[130] (⊠),[131] (○,●,□,■,◇),[110,111] (☆),[105] and (●,■, light-to-dark blue for $\eta = [0.001, 0.05, 0.1]$).[56]

ibility and temperature-dependent heat capacity, which are found to be non-negligible in the hypersonic regime, both LIA and DNS provide similar estimates of the relative influences of these factors.[56]

IV. CONCLUSIONS

This work investigates the fundamental physics of compressible turbulence interacting with planar shocks in hypersonic conditions through both theoretical and numerical approaches. The theoretical framework extends LIA.[47,55,56] to multi-component mixtures by incorporating the Combustion Toolbox[57], accounting for compressible and thermochemical effects. New results across a broad range of Mach numbers characterize the impact of upstream turbulence compressibility in the hypersonic regime, utilizing both LIA and DNS.

This section provides a final perspective on the shock-turbulence interaction problem, tracing its development from early theoretical approaches, such as LIA, to the latest advancements, including applications in hypersonic regimes. We summarize the main conclusions and key challenges, focusing on issues related to numerical discretization, the limitations of DNS, and the potential of LES. We also compare these methods with LIA, highlighting its most significant assumptions. Finally, we provide an outlook on future research directions in the field.

A. Concluding remarks

Regarding the canonical STI, various historical trends, summarized below, can be found in the literature since the pioneering work of Lee *et al.*[21–23] An important aim in the analysis of the generated data is to devise similarity scaling laws (e.g., see Refs. 63 and 112) to explain the observed amplification behavior as well as to identify shock regimes (e.g., see Refs. 37 and 64). Moreover, from an application perspective, fundamental studies can be used to devise or improve predictive models, as exemplified by several authors.[24–34,135] One common feature of the CFD studies discussed in Sec. III A, excluding the reacting STI, is the assumption of a constant specific heat capacity. In order to extend the relevance to hypersonic flows, temperature dependence of this property must be considered in either a thermally perfect gas (for lower enthalpy and low Knudsen numbers) or a thermally non-perfect gas, where chemical- and thermal non-equilibrium effects become significant. In this work, the latter topic has been discussed in the context of the canonical STI.

1. *Challenges of numerical discretization*

Owing to the multi-scale character of turbulent flows, minimal numerical dissipation proves necessary for an accurate and computationally efficient representation of high-wavenumber dynamics in shock-turbulence interaction. While the seminal works on the topic did not consider specific shock treatment in their studies which was possible due to the low shock Mach numbers ($\mathcal{M}_1 < 1.5$),

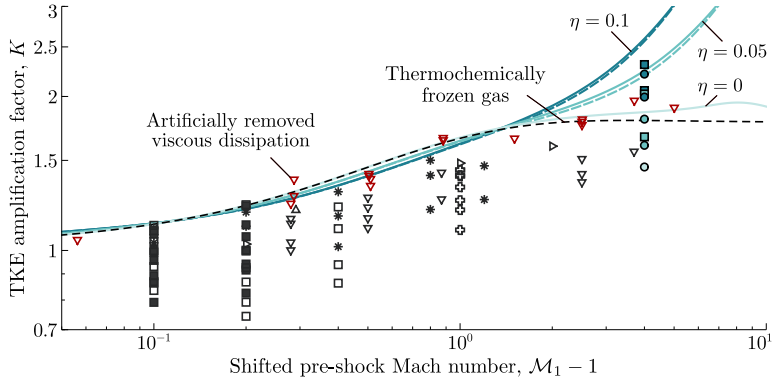

FIG. 12. TKE amplification factor K as a function of $\mathcal{M}_1 - 1$. The dashed lines correspond to the value of K assuming that the post-shock gas is thermochemically frozen. The symbols represent direct numerical simulations from other studies: (▷),[22,85] (△), [72] (▽),[37,46] (∗),[112] (✠), [130] (○,●,□,■,◇),[110,111] and (◍,◨, light-to-dark blue for $\eta = [0.001, 0.05, 0.1]$).[56] The red-hollow triangles (▽) represent the values from Larsson *et al.*[37] with artificially removed viscous dissipation.

increasing $\mathcal{M}_1$ requires alternative methods which are either shock capturing or shock-fitting. Shock capturing methods have received wider attention in the literature. They rely on the local addition of extra numerical dissipation to the solution either by upwinding the numerical scheme or by considering artificial flow properties. As the introduction of numerical dissipation has the side effect of damping turbulence fluctuations, confining its application to cells containing discontinuities is paramount to retaining accuracy in the flow description. This problem has motivated the development of improved shock sensors able to discern when the solution becomes discontinuous. In this context, a common solution is to deploy hybrid schemes, which use skew-symmetric or low-dissipation schemes in smooth regions of the flow and shock-capturing schemes for stencils that intersect discontinuities.

Shock-fitting techniques eliminate the need for shock sensors and have been used in the literature to investigate stronger shocks. The rationale behind their application is that the method removes the need to have very fine cells in the shock region which can become very stringent when the shock front corrugation is high. However, these methods are often associated with very high computational costs that is usually untenable on computational grids that are fine enough to support turbulence.

The simple geometrical features of the STI problem have favored the use of high-order numerics, which ensure high-computational intensity per grid point, for the discussed calculations, while relatively fewer studies have addressed the setup with low-order numerics, which are usually better suited for complex geometries and unstructured grids.[35,99,101] Additional work on finite-volume and low-order schemes would be valuable for extending the discussed findings to more complex configurations.

2. *Direct numerical simulations and their limits*

Direct numerical simulations have been the primary tool used to gain fundamental understanding of the canonical STI. Experimental methods are limited due to the difficulty of measuring pre- and post-shock states while controlling the shock wave position. In contrast, DNS allows precise control over the flow and several variations of the setup have been considered over the years. Key parameters investigated in these simulations, besides the Reynolds number and convective Mach number of the incoming flow, include the properties of the incoming turbulence, namely the intensity of the vortical fluctuations, entropy, and acoustic fluctuations.

The main limitation of the DNS methodology stands in its high computational cost. In fact, the computational grid that is utilized to discretize the Navier–Stokes equations must be fine enough to correctly describe all the scales of the flow (except for the shock itself) and large enough to accommodate a sufficient number of integral length scales. Moreover, the presence of the shock wave modifies the small scales of the flow by reducing their size and increasing their anisotropy. The parameter that mainly determines the computational cost of a configuration is the Taylor microscale Reynolds, Re_λ, of the incoming turbulence. This dependency is readily justified by the broadening of the turbulence spectrum at higher Reynolds numbers. Note that current boundaries of this phase space explored with DNS pertain Re_λ between approximately 40 and 70. These values are quite low if we consider that a proper inertial rage of turbulence is usually observed for $\mathrm{Re}_\lambda \sim 100$.

The cost of a DNS of STI also depends on the Mach number of the incoming flow. In particular, the ratio of Kolmogorov length scales ($\eta_{k,2}/\eta_{k,1}$) between the upstream and downstream turbulence scales as

$$\frac{\eta_{k,2}}{\eta_{k,1}} \sim \mathcal{P}\mathcal{T}^{11/8}, \tag{40}$$

where $\mathcal{P}$ and $\mathcal{T}$ represent the pressure and temperature ratios across the shock.[46] It can easily be inferred that the worst-case scenario happens at the border of the hypersonic regime around Mach 5.

The turbulence Mach number, and in particular its ratio with the convective Mach number, also contribute to the computational cost. This parameter linearly affects the integration time window necessary to capture the interaction. A small value of $\mathcal{M}_t/\mathcal{M}_1$, typical of hypersonic STI, results in a strong separation of scales between the integral time scales of turbulence and the convective time scales. Considering that the size of the computational domain is usually of the order of the integral scale of the turbulence, a large number of flow-through times is required to describe one eddy turnover time of the incoming flow. Conversely, a high $\mathcal{M}_t/\mathcal{M}_1$ limits the computational cost of the calculations by reducing the separation of time scales between mean advection and turbulence.

Moving toward the hypersonic regime and considering stronger shock waves, the inclusion of high-temperature phenomena, such as chemical and thermal non-equilibrium, will also increase the computational cost of the calculations by augmenting the set of transport equations that need to be solved. To have a sense of the impact of the inclusion of these phenomena in the calculations, one could consider that the typical ratio of computational costs of a standard shock-capturing scheme scales with the number of unknowns to the power two or three. However, the specifics of the numerical methods deployed during the numerical simulations must be considered to identify a proper scaling.

3. Large eddy simulations

Improving dramatically the computational tractability of scale-resolving simulations, large-eddy simulation (LES) requires significantly fewer degrees of freedom than direct numerical simulation. As the LES paradigm involves resolving only the largest scales of turbulent motion, physical modeling of the effect of small-scale processes on the resolved quantities proves necessary. To enable predictive LES in the context of supersonic canonical STI, in particular, three crucial elements have been identified. Firstly, dynamic modeling was shown to provide significant improvement in the prediction of filtered Reynolds stresses as compared to both coarsened DNS (i.e., without an explicit SGS model) and static LES modeling. Secondly, ensuring that the computational grid is sufficiently fine in the vicinity of the shock to directly resolve corrugations was shown to be crucial for predictive simulations of second-order statistics. Finally, the inclusion of the SGS fluxes only in smooth regions of the flow, i.e., those cells in which the hybrid scheme reverts to a central discretization, prevents artificial damping of turbulent fluctuations. However, the development and evaluation of LES capabilities for shock-turbulence interaction in the hypersonic regime remain essentially absent from the literature, even for calorically perfect gases. In light of the canonical STI's relevance to propulsion-system design and broader aerospace applications, more sophisticated LES models will be required not only for subgrid chemistry but also advective transport of both scalars (species, temperature, etc.) and momentum, particularly for high-Mach conditions.

4. CFD VS. LIA

LIA has been used alongside DNS as it provides a theoretical framework for comparing and understanding behavioral trends in STI. Historically, challenges in achieving a fair comparison between LIA and DNS have led to very different results between both methods, particularly regarding the amplification of the Reynolds stresses. These differences were attributed mainly to variations in the definition of the post-shock (or post-interaction) location and the impact of viscous effects. To address this, viscous decay was compensated by extrapolating the DNS solution behind the shock region (defined based on the bounds of shock oscillations) back to the mean shock location.[37,46,85] This resulted in better agreement between the two frameworks. An important milestone in canonical STI studies is the reconciliation between DNS and LIA, which was achieved by considering the ratio of laminar shock thickness to the pre-shock Kolmogorov length scale (the scale-separation parameter) as a reference scaling parameter. When this parameter gets closer to zero, DNS predictions of Reynolds stresses and vorticity variance amplifications converge towards LIA predictions. Building on this, LIA has enabled to increase the range of Re_λ accessible in post-shock turbulence studies by its use in generating a shock-processed state[113,114] (also referred to as shock-LIA). Furthermore, LIA can be used in a predictive sense over a wide range of conditions which in turn would allow the improvement of, for instance, RANS models (see, e.g., Refs. 25 and 29).

In what concerns the hypersonic regime, we have explored the potential of LIA under the following considerations: i) the upstream turbulence may consist of small-amplitude perturbations of various types, such as rotational, entropic, and acoustic; ii) the thermochemical non-equilibrium region may involve processes like vibrational excitation, molecular dissociation/recombination, and ionization. The latter assumes that the characteristic size of the turbulence is much larger than the non-equilibrium length, a condition strongly influenced by the nature of the turbulence (modal composition), the

shock Mach number, and the upstream flow conditions, as evidenced by the flight-altitude effects commented on before. This is due to the strong temperature dependence of relaxation processes and chemical kinetics.[47] From a practical perspective, the LIA model presented in this work assumes that the high-frequency part of the turbulence spectrum can be neglected. It should be noted that the opposite limit, which is not covered in this section, involves separating the interaction between turbulence and an inert shock from the study of post-shock turbulence evolution in a still-compressing non-equilibrium flow. This approach, as explored in Huete *et al.*[136] for detonation-turbulence interaction, is left for future investigation.

B. Outlook

Based on the discussion presented in this review, several insights can be drawn regarding the specific numerical methods, including DNS and LES:

- **Numerical methods for STI.** The transition to the hypersonic regime introduces even greater challenges for numerical methods, as increasingly intense shocks demand higher precision in their identification to preserve the stability of the calculation. At the same time, the appearance of eddy shocklets will blur the boundaries of the flow conditions, complicating when numerical dissipation must be added. The hybrid schemes appear for now a valuable solution to the problem, though additional work in shock sensors is necessary to minimize numerical dissipation without compromising stability.

- **Direct numerical simulations.** Future calculations must be performed well into the hypersonic regime, incorporating high-Reynolds-number incoming turbulence with a wide inertial subrange. High-temperature effects must also be included to shed light on the interaction between thermal and chemical relaxation and the highly anisotropic turbulence downstream of the shock wave. Exascale supercomputers must be leveraged to achieve this goal.

- **Large eddy simulations.** New sub-grid-scale models must be developed to enable prediction post-shock turbulence with numerical solution of the the filtered Navier–Stokes equations, particularly for high-enthalpy hypersonic flows. In this context, new DNS databases at high Reynolds and Mach numbers can facilitate their development and evaluation via *a priori* analysis.

ACKNOWLEDGMENTS

CH and ACL work has been partially supported by projects PID2022-139082NB-C51 and TED2021-129446B-C41 funded by MCIN/AEI. MDR acknowledges the CINECA award under the ISCRA initiative, for the availability of high-performance computing resources and support. C.W. acknowledges support by the National Science Foundation Graduate Research Fellowship Program under Grant No. DGE2146755. JH work was supported by the "DLR DAAD Research Fellowship Programme".

DATA AVAILABLITY

The data that support the findings of this study are available from the corresponding author upon reasonable request.

REFERENCES

[1]J. Longo, K. Hannemann, and V. Hannemann, DLR Report **2**, 1 (2007).
[2]G. Settles and L. Dodson, AIAA journal **32**, 1377 (1994).
[3]V. Theofilis, S. Pirozzoli, and P. Martin, Theoretical and Computational Fluid Dynamics **36**, 1 (2022).
[4]H. Olivier and S. Gu, VKI Lecture Series: Flow Characterization and Modeling of Hypersonic Wind Tunnels, von Karman Inst. for Fluid Dynamics STO-EN AVT-325-01, Sint-Genesius-Rode, Belgium (2018).
[5]S. Gu and H. Olivier, Progress in Aerospace Sciences **113**, 100607 (2020).
[6]E. Johnsen, J. Larsson, A. Bhagatwala, W. Cabot, P. Moin, B. Olson, P. S. Rawat, S. Shankar, B. Sjögreen, H. Yee, *et al.*, Journal of Computational Physics **229**, 1213 (2010).
[7]J. Larsson, S. Lele, and P. Moin, Annual research briefs , 47 (2007).
[8]M. Di Renzo, L. Fu, and J. Urzay, Computer Physics Communications **255**, 107262 (2020).
[9]M. Di Renzo and S. Pirozzoli, Computer Physics Communications **261**, 107733 (2021).
[10]P. Volpiani, Shock Waves **31**, 361 (2021).
[11]M. Bernardini, D. Modesti, F. Salvadore, S. Sathyanarayana, G. Della Posta, and S. Pirozzoli, Computer Physics Communications **285**, 108644 (2023).
[12]S. Sathyanarayana, M. Bernardini, D. Modesti, S. Pirozzoli, and F. Salvadore, arXiv preprint arXiv:2304.05494 10.1016/j.jpdc.2024.104993 (2023).
[13]F. De Vanna, F. Avanzi, M. Cogo, S. Sandrin, M. Bettencourt, F. Picano, and E. Benini, Computer Physics Communications **287**, 108717 (2023).
[14]F. De Vanna, M. Bernardini, F. Picano, and E. Benini, International Journal of Heat and Fluid Flow **98**, 109071 (2022).
[15]D. Passiatore, L. Sciacovelli, P. Cinnella, and G. Pascazio, Physical Review Fluids **8**, 044601 (2023).
[16]G. Della Posta, M. Blandino, D. Modesti, F. Salvadore, and M. Bernardini, Journal of Fluid Mechanics **974**, A44 (2023).
[17]M. Di Renzo, C. T. Williams, and S. Pirozzoli, Phys. Rev. Fluids **9**, 033401 (2024).
[18]M. Di Renzo and J. Urzay, Journal of Fluid Mechanics **912**, A29 (2021).

[19]J. Larsson, V. Kumar, N. Oberoi, M. Di Renzo, and S. Pirozzoli, AIAA journal **60**, 2767 (2022).
[20]S. Zhang, X. Li, J. Zuo, J. Qin, K. Cheng, Y. Feng, and W. Bao, Progress in Aerospace Sciences **119**, 100646 (2020).
[21]S. Lee, P. Moin, and S. Lele, *Interaction of isotropic turbulence with a shock wave*, Tech. Rep. (Stanford University CA Dept of Mechanical Engineering, 1992).
[22]S. Lee, S. Lele, and P. Moin, Journal of Fluid Mechanics **251**, 533 (1993).
[23]S. Lee, Annual Research Briefs (1993).
[24]V. K. Veera and K. Sinha, Physics of fluids **21**, 10.1063/1.3073744 (2009).
[25]K. Sinha, Journal of fluid mechanics **707**, 74 (2012).
[26]R. Quadros and K. Sinha, International Journal of Heat and Fluid Flow **61**, 626 (2016).
[27]R. Quadros, K. Sinha, and J. Larsson, J. Fluid Mech **796**, 113 (2016).
[28]S. Karl, J. Hickey, and F. Lacombe, in *International Symposium on Shock Waves* (Springer, 2017) pp. 511–517.
[29]J. Vemula and K. Sinha, Journal of Turbulence **18**, 653 (2017).
[30]S. Roy, U. Pathak, and K. Sinha, AIAA Journal **56**, 342 (2018).
[31]N. Braun, *An LES and RANS Study of the Canonical Shock-Turbulence Interaction*, Ph.D. thesis, California Institute of Technology (2018).
[32]S. Roy and K. Sinha, AIAA Journal **57**, 3624 (2019).
[33]J. Vemula and K. Sinha, International Journal of Heat and Fluid Flow **85**, 108680 (2020).
[34]F. Lacombe, S. Roy, K. Sinha, S. Karl, and J. Hickey, AIAA Journal **59**, 526 (2021).
[35]S. Jamme, J.-B. Cazalbou, F. Torres, and P. Chassaing, Flow, Turbulence and Combustion **68**, 227 (2002).
[36]N. Grube, E. Taylor, and P. Martin, in *49th AIAA Aerospace Sciences Meeting including the New Horizons Forum and Aerospace Exposition* (2011) p. 480.
[37]J. Larsson, I. Bermejo-Moreno, and S. Lele, Journal of Fluid Mechanics **717**, 293 (2013).
[38]L. Kovasznay, Journal of the Aeronautical Sciences **20**, 657 (1953).
[39]H. Ribner, NACA Report , 1164 (1954).
[40]H. Ribner, *Shock-turbulence interaction and the generation of noise*, Tech. Rep. (National Aeronautics and Space Administration, Cleveland OH Lewis Research Center, 1955).
[41]F. Moore, *Unsteady oblique interaction of a shock wave with a plane disturbance*, Vol. 1165 (National Advisory Committee for Aeronautics, 1953).
[42]C.-T. Chang, Journal of the Aeronautical Sciences **24**, 675 (1957).
[43]S. Lele, Physics of Fluids A: Fluid Dynamics **4**, 2900 (1992).
[44]C. Cambon, G. Coleman, and N. Mansour, Journal of Fluid Mechanics **257**, 641 (1993).
[45]L. Jacquin, C. Cambon, and E. Blin, Physics of Fluids A: Fluid Dynamics **5**, 2539 (1993).
[46]J. Larsson and S. Lele, Physics of fluids **21**, 126101 (2009).
[47]C. Huete, A. Cuadra, M. Vera, and J. Urzay, Physics of Fluids **33**, 086111 (2021).
[48]T. Jackson, M. Hussaini, and H. Ribner, Physics of Fluids A: Fluid Dynamics **5**, 745 (1993).
[49]C. Huete, A. L. Sánchez, and F. A. Williams, Physics of Fluids **25**, 076105 (2013).
[50]A. Cuadra, C. Huete, and M. Vera, Journal of Fluid Mechanics **903**, 10.1017/jfm.2020.651 (2020).
[51]T. Jin, K. Luo, Q. Dai, and J. Fan, AIAA Journal **54**, 419 (2016).
[52]C. Huete, T. Jin, D. Martínez-Ruiz, and K. Luo, Physical Review E **96**, 053104 (2017).
[53]K. Iwata, S. Suzuki, R. Kai, and R. Kurose, Physics of Fluids **35**, 10.1063/5.0144624 (2023).
[54]S. Suzuki, K. Iwata, R. Kai, and R. Kurose, Proceedings of the Combustion Institute **40**, 105337 (2024).
[55]A. Cuadra, M. Vera, M. Di Renzo, and C. Huete, in *AIAA SciTech 2023 Forum, AIAA paper 2023–0075* (2023).
[56]A. Cuadra, C. T. Williams, M. Di Renzo, and C. Huete, *Compressibility and vibrational-excitation effects in hypersonic shock-turbulence interaction*, Tech. Rep. (Summer Program Proceedings, Center for Turbulence Research, Stanford University, 2024).
[57]A. Cuadra, C. Huete, and M. Vera 10.48550/arXiv.2409.15086 (2024), arXiv:2409.15086 [physics.chem-ph].
[58]G. V. Candler, Annual Review of Fluid Mechanics **51**, 379 (2019).
[59]C. Park, *Nonequilibrium Hypersonic Aerothermodynamics* (Wiley, 1990).
[60]S. Ghosh and P. P. Kerkar, in *AIAA SCITECH 2022 Forum* (2022) p. 2015.
[61]C. Williams, M. Di Renzo, and P. Moin, *Computational Framework for Direct Numerical Simulation of Shock-Turbulence Interaction in Thermochemical Nonequilibrium*, Tech. Rep. (Annual Research Briefs, Center for Turbulence Research, 2022).
[62]C. Williams, M. Di Renzo, J. Urzay, and P. Moin, Journal of Computational Physics **509**, 113040 (2024).
[63]D. Donzis, Physics of Fluids **24**, 011705 (2012).
[64]D. Donzis, Physics of Fluids **24**, 126101 (2012).
[65]B. J. McBride, *NASA Glenn coefficients for calculating thermodynamic properties of individual species* (National Aeronautics and Space Administration, John H. Glenn Research Center, 2002).
[66]A. Cuadra, C. Huete, and M. Vera, Combustion Toolbox: A MATLAB-GUI based open-source tool for solving gaseous combustion problems (2024), version 1.1.0.
[67]A. Cuadra, *Development of a wide-spectrum thermochemical code with application to planar reacting and non-reacting shocks*, PhD thesis, Universidad Carlos III de Madrid (2023).
[68]S. Gordon and B. J. McBride, No. NAS 1.61:1311 (1994).
[69]M. R. Petersen and D. Livescu, Physics of Fluids **22**, 116101 (2010).
[70]B. Bottin, Progress in Aerospace Sciences **36**, 547 (2000).
[71]O. Askari, Journal of Energy Resources Technology **140**, 10.1115/1.4037688 (2018).
[72]K. Mahesh, S. Lele, and P. Moin, Journal of Fluid Mechanics **334**, 353 (1997).
[73]R. Quadros, K. Sinha, and J. Larsson, J. Fluid Mech **796**, 113 (2016).
[74]C. Huete, J. Wouchuk, and A. Velikovich, Phys. Rev. E **85**, 026312 (2012).
[75]M. Smart, The Aeronautical Journal **111**, 605 (2007).
[76]M. Di Renzo, Computer Physics Communications **272**, 108247 (2022).
[77]C. Williams, M. Di Renzo, and J. Urzay, *Two-temperature extension of the HTR solver for hypersonic turbulent flows in thermochemical nonequilibrium*, Tech. Rep. (Center for Turbulence Research Annual Research Briefs, 2021).
[78]T. J. Poinsot and S. K. Lele, Journal of Computational Physics **101**, 104 (1992).
[79]M. Cavcar, Anadolu University, Turkey **30**, 1 (2000).
[80]S. Pirozzoli, Annual review of fluid mechanics **43**, 163 (2011).
[81]P. Moin and K. Mahesh, Annual review of fluid mechanics **30**, 539 (1998).
[82]A. Harten, B. Engquist, S. Osher, and S. R. Chakravarthy, Journal of computational physics **131**, 3 (1997).
[83]G.-S. Jiang and C.-W. Shu, Journal of computational physics **126**, 202 (1996).
[84]L. Fu, X. Y. Hu, and N. A. Adams, Journal of Computational Physics **305**, 333 (2016).
[85]S. Lee, S. Lele, and P. Moin, Journal of Fluid Mechanics **340**, 225 (1997).
[86]G.-Y. Zhao, M.-B. Sun, and S. Pirozzoli, Computers & Fluids **199**, 104439 (2020).
[87]J. von Neumann and R. D. Richtmyer, Journal of applied physics **21**, 232 (1950).

[88]A. Jameson, W. Schmidt, and E. Turkel, in *14th fluid and plasma dynamics conference* (1981) p. 1259.
[89]A. W. Cook, Physics of fluids **19** (2007).
[90]A. Mani, J. Larsson, and P. Moin, Journal of Computational Physics **228**, 7368 (2009).
[91]M. Onofri and R. Paciorri, *Shock fitting: classical techniques, recent developments, and memoirs of Gino Moretti* (Springer, 2017).
[92]J. Sesterhenn, J. Dohogne, and R. Friedrich, Comptes Rendus Mécanique **333**, 87 (2005).
[93]P. Rawat and X. Zhong, in *48th AIAA Aerospace Sciences Meeting Including the New Horizons Forum and Aerospace Exposition* (2010) p. 114.
[94]P. Rawat and X. Zhong, in *49th AIAA Aerospace Sciences Meeting including the New Horizons Forum and Aerospace Exposition* (2011) p. 649.
[95]X. Wang and X. Zhwang2012highong, in *50th AIAA Aerospace Sciences Meeting including the New Horizons Forum and Aerospace Exposition* (2012) p. 1243.
[96]S. Pirozzoli, Journal of Computational Physics **230**, 2997 (2011).
[97]C. A. Kennedy and A. Gruber, Journal of Computational Physics **227**, 1676 (2008).
[98]S. K. Lele, Journal of computational physics **103**, 16 (1992).
[99]F. Ducros, V. Ferrand, F. Nicoud, C. Weber, D. Darracq, C. Gacherieu, and T. Poinsot, Journal of Computational Physics **152**, 517 (1999).
[100]S. Hickel, C. Egerer, and J. Larsson, Physics of Fluids **26**, 106101 (2014).
[101]J. Hoste, *Assessment of scale resolving turbulence models in the TAU code for canonical shock-turbulence interaction*, Tech. Rep. DLR-FB-2020-28. 169 S (DLR, 2023).
[102]C. Wang and C.-W. Shu, Journal of Computational Physics **229**, 8823 (2010).
[103]D. S. Hoskin, R. L. Van Heyningen, N. C. Nguyen, J. Vila-Pérez, W. L. Harris, and J. Peraire, Progress in Aerospace Sciences **146**, 100999 (2024).
[104]F. M. D'Afiero, M. Mihaescu, and A. Hanifi, Physics of Fluids **36** (2024).
[105]N. Grube and M. Martín, Journal of Fluid Mechanics **958**, A1 (2023).
[106]X. Gao, I. Bermejo-Moreno, and J. Larsson, Journal of Fluid Mechanics **895**, 10.1017/jfm.2020.292 (2020).
[107]A. Kusuhata, K. Tanaka, T. Watanabe, K. Nagata, and A. Sasoh, Physics of Fluids **35**, 10.1063/5.0158309 (2023).
[108]K. Tanaka, T. Watanabe, K. Nagata, A. Sasoh, Y. Sakai, and T. Hayase, Physics of Fluids **30**, 10.1063/1.5019867 (2018).
[109]K. Tanaka, T. Watanabe, and K. Nagata, Physics of Fluids **32**, 10.1063/5.0019784 (2020).
[110]C. Chen and D. Donzis, Journal of Fluid Mechanics **870**, 813 (2019).
[111]C. Chen and D. Donzis, AIAA Journal **60**, 6235 (2022).
[112]J. Ryu and D. Livescu, Journal of Fluid Mechanics **756**, 10.1017/jfm.2014.477 (2014).
[113]D. Livescu and J. Ryu, Shock Waves **26**, 241 (2016).
[114]D. Livescu and Z. Li, in *AIP Conference Proceedings* (AIP Publishing LLC, 2017) p. 150009.
[115]I. Bermejo-Moreno, Annu. Res. Briefs, Center for Turbulence Research , 247 (2009).
[116]M. Pino Martín, U. Piomelli, and G. V. Candler, Theoretical and Computational Fluid Dynamics **13**, 361 (2000).
[117]B. Vreman, B. Geurts, and H. Kuerten, Applied scientific research **54**, 191 (1995).
[118]A. Saghafian, *High-fidelity simulations and modeling of compressible reacting flows* (Stanford University, 2014).
[119]E. Garnier, P. Sagaut, and M. Deville, Computers & fluids **31**, 245 (2002).
[120]M. Germano, U. Piomelli, P. Moin, and W. Cabot, Physics of Fluids A: Fluid Dynamics **3**, 1760 (1991).
[121]P. Moin, K. Squires, W. Cabot, and S. Lee, Physics of Fluids A: Fluid Dynamics **3**, 2746 (1991).
[122]I. Bermejo-Moreno, J. Larsson, and S. Lele, Annual Research Briefs , 209 (2010).
[123]N. Braun, D. Pullin, and D. Meiron, Journal of Fluid Mechanics **858**, 500 (2019).
[124]N. Braun, D. Pullin, and D. I. Meiron, Journal of Computational Physics **361**, 231 (2018).
[125]G. Erlebacher, M. Hussaini, C. Speziale, and T. Zang, ICASE/-NASA Langley Research Center (1990).
[126]C. G. Speziale, G. Erlebacher, T. Zang, and M. Hussaini, *On the subgrid-scale modeling of compressible turbulence*, Tech. Rep. (1987).
[127]J. Urzay and M. Di Renzo, Annual Research Briefs, Center for Turbulence Research, Stanford University , 7 (2020).
[128]M. P. Martın and G. V. Candler, Physics of Fluids **11**, 2765 (1999).
[129]C. Williams, *Subgrid-scale modeling of turbulence-chemistry interaction for hypersonic boundary layers in chemical nonequilibrium*, Tech. Rep. (Annual Research Briefs, Center for Turbulence Research, Stanford University, 2023).
[130]Y. Tian, F. Jaberi, Z. Li, and D. Livescu, Journal of Fluid Mechanics **829**, 551 (2017).
[131]R. Boukharfane, Z. Bouali, and A. Mura, Shock Waves **28**, 1117 (2018).
[132]X. Gao, *Direct Numerical Simulation of Mixing and Combustion Under Canonical Shock Turbulence Interaction*, Ph.D. thesis, University of Southern California (2020).
[133]P. Dimotakis, Journal of Fluid Mechanics **409**, 69 (2000).
[134]B. McManamen, D. Donzis, S. North, and R. Bowersox, Journal of Fluid Mechanics **913**, 10.1017/jfm.2020.1161 (2021).
[135]Y. Sethuraman and K. Sinha, AIAA Journal **58**, 3076 (2020).
[136]C. Huete, A. L. Sánchez, and F. A. Williams, Physics of Fluids **26**, 116101 (2014).